International Journal of Greenhouse Gas Control 94 (2020) 102923

Contents lists available at ScienceDirect

International Journal of Greenhouse Gas Control

journal homepage: www.elsevier.com/locate/ijggc

Geomechanical and petrographic assessment of a CO_2 storage site: Application to the Acorn CO_2 Storage Site, offshore United Kingdom

Michael J. Allen*, Daniel R. Faulkner, Richard H. Worden, Elliot Rice-Birchall, Nikolaos Katirtsidis, James E.P. Utley

Department of Earth, Ocean and Ecological Sciences, University of Liverpool, Liverpool, UK

ARTICLE INFO

Keywords:
CO_2 geological storage
Moray Firth
Geomechanics
Petrography
ACT-Acorn
Geology

ABSTRACT

Extraction or injection of fluids within the subsurface causes fluctuations of fluid pressures and thus stress conditions. It is paramount to have knowledge of the geomechanical strength of a system's lithologies, and the factors that control it, in order to maintain optimal conditions during extraction/injection. If the yield strengths of the reservoir or caprock are overcome, particularly in the near-wellbore region where stress is amplified, these fluctuations could potentially compromise the system, through compactional or dilatational failure. Here we have used a novel combination of methods to determine the geomechanical and petrographic properties of the reservoir and caprock lithologies to assess suitability of the proposed Acorn CO_2 Storage Site, offshore north-east Scotland, for long-term injection and storage of CO_2.

The Acorn CO_2 Storage Site has a highly porous and transmissible sandstone reservoir, with bulk mineralogy that will be stable under CO_2-rich conditions, making it ideal for receiving at least 152 MT CO_2 injected over ~20 years and storage of > 1000 years post-injection, as part of the ACT-Acorn Development Plan. However, due to the high porosity and low cementation of the sandstone reservoir, it has low yield strength and is vulnerable to disaggregation and porosity-reduction if injection rates are too high and stress/pressure conditions exceed their yield strength. The results presented here provide quantitative constraints on the porosity reduction expected should yield occur and place limits on CO_2 injection rates. The shale caprock, with a high swelling clay content and very low permeability, present ideal Carbon Capture and Storage seal properties.

1. Introduction

During production of fluid from reservoirs, extraction reduces reservoir fluid pressure, potentially causing subsidence of both the reservoir and overlying caprock, such as the Ekofisk oil field, Norway (Sulak and Danielsen, 1988) and the Groningen gas field, Netherlands (Thienen-Visser et al., 2015). During large-scale CO_2 injection, the pore fluid within the reservoir will be re-pressurised, potentially beyond that of its original conditions pre-hydrocarbon production, i.e. the In Salah CO_2 Storage Project, Algeria (Ringrose et al., 2013). With these fluctuations of pressure and stress conditions within the reservoir and, by association, the caprock, deformation and failure of the reservoir or caprock may occur, resulting in a change in rock properties such as porosity, permeability and injectivity potential (Chan and Zoback, 2002; Segall, 1985). The geomechanical strength of a rock is fundamentally controlled by its mineralogy and texture, i.e., the way the minerals are fitted together (Jaeger et al., 2007). Constraining geomechanical strength is important as it controls (i) how much, and at what pressure, CO_2 can be injected, (ii) the conditions to be maintained to preserve borehole integrity, and (iii) infrastructure concerns such as filtration units and subsurface sand screens (Hoffman et al., 2017; Mathisen et al., 2007; Zoback, 2007).

The geomechanical properties of all parts of a petroleum system are typically derived from downhole wireline log data, seismic surveys and downhole pressure tests (Rider, 2002; Zoback, 2007). Using core samples retrieved during petroleum exploration and field development, this study has undertaken direct measurement of rock strength to provide complete yield and post-yield curves for the reservoir. This study has investigated the tensile strength and the yield strength of the Captain Sandstone reservoir, the Rodby Shale caprock and the mid-reservoir Sola Shale, located within the Acorn CO_2 Storage Site, offshore in the Inner Moray Firth Basin, see Fig. 1. Injection will take place into the

* Corresponding author at: University of Liverpool, School of Environmental Sciences, Jane Herdman Building, 4 Brownlow Street, Liverpool, Merseyside, L69 3GP, UK.

E-mail addresses: mjallen@liverpool.ac.uk (M.J. Allen), faulkner@liverpool.ac.uk (D.R. Faulkner), rworden@liverpool.ac.uk (R.H. Worden), sgericeb@student.liverpool.ac.uk (E. Rice-Birchall), N.Katirtsidis@liverpool.ac.uk (N. Katirtsidis), etrsi@liverpool.ac.uk (J.E.P. Utley).

https://doi.org/10.1016/j.ijggc.2019.102923
Received 10 May 2019; Received in revised form 22 November 2019; Accepted 22 November 2019

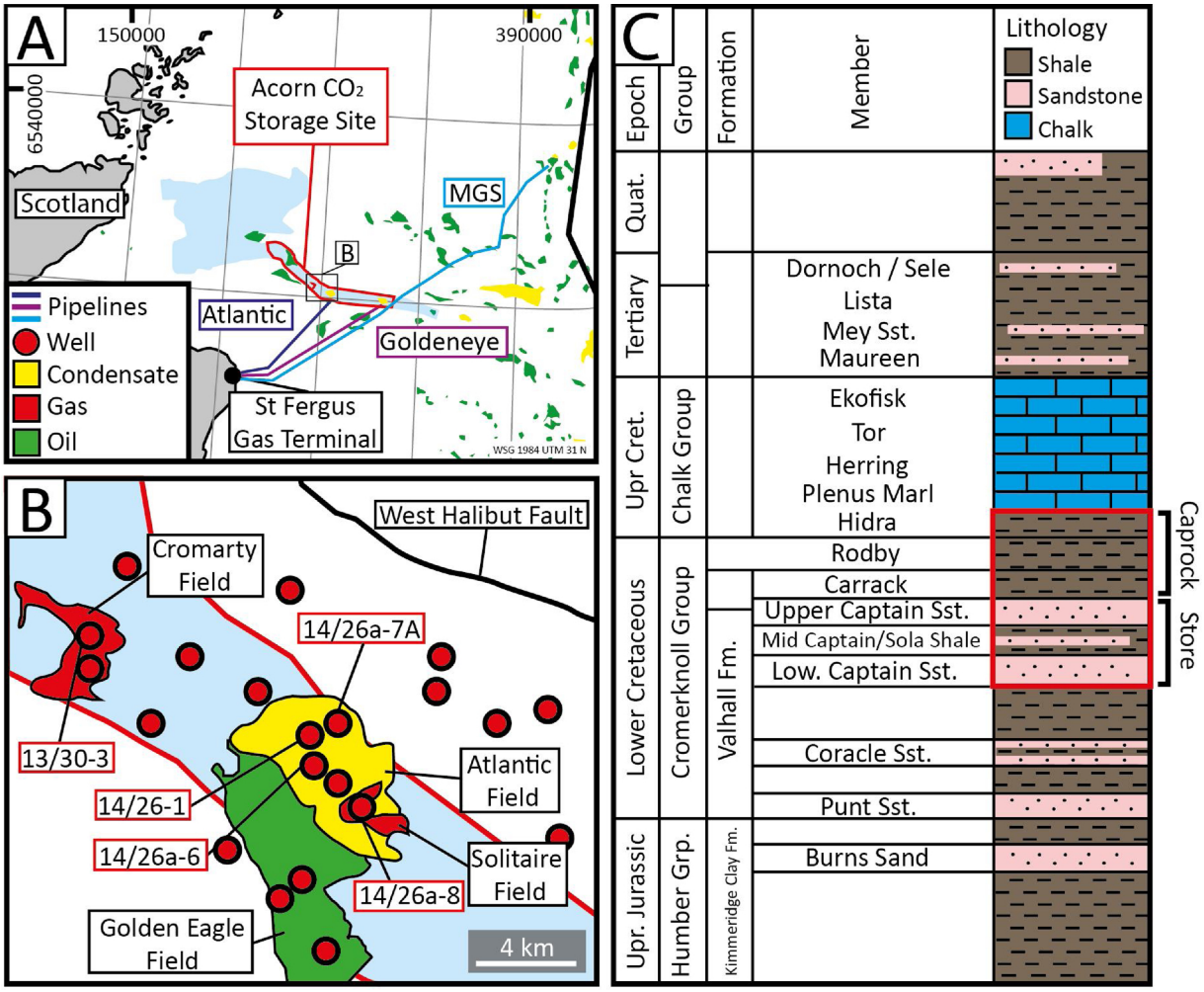

Fig. 1. Location of Acorn CO_2 Storage Site study area and its stratigraphy. [A] A map of the western North Sea with extent of the Captain Sandstone Member in blue with the Acorn CO_2 Storage Site highlighted in red. Hydrocarbon fields and pipelines extending from the St Fergus Gas Terminal are included. [B] Region of study within the Atlantic/Solitaire Fields, sampled wells are labelled. [C] The lithostratigraphy of the Acorn CO_2 Storage Site with site lithologies highlighted in red.

saline aquifer within the Captain Sandstone and contained by residual trapping, dissolution within formation fluids and structural trapping by the overlying shale caprock lithologies for storage for a minimum of 1000 years (Pale Blue Dot Energy, 2018a). From these data, the yield under any stress conditions can be quantitatively predicted. For the caprock, the tensile strength was measured. The rock strength data have been related to data from petrographic mineralogical and textural analyses performed on core samples in order to develop a predictive understanding of subsurface rock strength and its controls. Permanent deformation within reservoirs and surrounding wellbores can become a serious problem in a number of injection or extraction scenarios (Pijnenburg et al., 2019; Vasco et al., 2010). Geomechanical analyses involving knowledge of the in situ stress field and the full post-yield mechanical behaviour could, and perhaps should, be used in general to gain a clearer picture on the predicted porosity and mechanical evolution and the resultant subsidence and uplift.

This study was motivated by the Accelerating Carbon Technologies (ACT) Acorn Carbon Capture and Storage (CCS) Project, under the ERA–NET Horizon 2020 programme, project 271500, and was jointly funded by the Department for Business, Energy and Industrial Strategy, United Kingdom; the Research Council of Norway; Netherlands Enterprise Agency. The project aimed to implement a low cost, scalable full chain CCS hub that will capture CO_2 emissions from the St Fergus Gas Terminal in North East Scotland and subsequently store the CO_2 at an offshore storage site under the North Sea (Alcade et al., 2019; Pale Blue Dot Energy, 2018b). The project was comprised of both technical and non-technical activities including scientific research with the aim to develop the technical specifications for an ultra-low cost, integrated CCS hub that can be scaled up at marginal cost (Pale Blue Dot Energy, 2018b).

1.1. Geological background and tectonic history

The following section summarises, in ascending order, the key aspects of the lithostratigraphy and geology of the Acorn CO_2 Storage Site and its bounding lithologies. This lithostratigraphy is illustrated in Fig. 1C.

The Lower Cretaceous Captain Sandstones and the Sola, Carrack and Rodby Shales are the key storage and caprock lithologies, respectively, for the Acorn CO_2 Storage Site and will be described in detail below. At the top of the Upper Jurassic, stratigraphically below the Acorn CO_2 Storage Site, lies the Kimmeridge Clay Formation, composed dominantly of marine hemipelagic mudstones, which is the hydrocarbon source rock for many petroleum fields in the region (Gallois, 2004; Kubala et al., 2003). This formation also contains sandstone intervals deposited as deep marine mass flows, which include the Burns Sand Member (Fraser et al., 2003). The Lower Cretaceous Cromer Knoll Group is composed of turbiditic sand units, which include the Punt, Coracle and Captain Sandstones, with hemipelagic shales occurring throughout, including the Mid-Captain Sola Shale, Carrack and Rodby

Shales (Copestake et al., 2003). Overlying the Storage Site is the Upper Cretaceous Chalk Group, which divides into: the Plenus Marl Formation, composed of black anoxic calcareous mudstones; the Hidra Formation, composed of argillaceous limestones, marls and mudstones; and the Ekofisk, Tor, Hod and Herring Formations, composed of limestone interbedded with claystone and marl beds (Surlyk et al., 2003). Up sequence, the Cenozoic is divided into: the Maureen Formation, composed of amalgamated gravity flow sands with reworked basinal chalk and interbedded siltstones; the Lista Shale, composed of marine basin / outer shelf mudstone interbedded with submarine gravity flow sandstones, which occur across the Outer Moray Firth and Central Graben, known as the Mey Sandstone Member, locally known as Andrew and Balmoral Sandstones (Ahmadi et al., 2003; Jones et al., 2003). At the top of the succession is the Quaternary Nordland Group, composed of undifferentiated mudstones, claystones and localised marls (Fyfe et al., 2003).

The Captain Sandstone fairway, the primary storage lithology, occurs as an elongate body of sand, shaped like a cooking pan, lying north west to south east, along the southern edge of the Halibut Horst (Fig. 1A and B). The Captain Sandstone regionally dips 1 to 2 ° to the south east with a steep ramp of 20 ° at its north western extent close to the West Halibut Fault. The Captain Sandstone has its widest extent in the north west and sub-crops at the seabed, while at its south eastern extent it is presently at depths in excess of 3660 m (Pale Blue Dot Energy, 2018a).

The Captain Sandstone can be subdivided into the Upper Captain and Lower Captain by the Mid-Captain Sola Shale (Sola Formation) (Fig. 1C). The Captain Sandstone Member is predominantly composed of thick-bedded, stacked, and amalgamated fine to medium grained sandstones deposited as suspension collapse from high density turbidity currents (Pinnock et al., 2003). The thickness of the full Captain Sandstone unit can be up to 143 m thick in the centre of the fairway but pinches out to the north and the south. On average, the thickness of the full unit is approximately 54 m and the thickness of the Mid-Captain Sola Shale (between the upper and lower sands) averages 15 m thick (Pale Blue Dot Energy, 2018a). On its upper boundary, the Captain Sandstone contains fining up-sequences and ripple cross-stratified thin beds and transitions into the overlying mudstones of the Sola and Rodby Shale (Pinnock et al., 2003). The Captain Sandstone is trapped and sealed by a three-way dip closure and stratigraphic pinch-out which is top-sealed by the overlying the Rodby Shale Member and the Hidra Chalk Group (Pinnock et al., 2003). The proposed location of the Acorn CO_2 Storage Site is an open saline aquifer within the Captain Sandstone Member, comprised of a sand fairway, 5 to 10 km wide, with a north-west to south-east orientation, bound by the Halibut Horst and South Halibut Shelf to the north.

The Captain Sandstone spans both the eastern Inner Moray Firth (IMF) and western Outer Moray Firth (OMF). The geological structure of the Moray Firth is typified by ENE-WSW-trending fault-defined horsts, basins and sub-basins generated through a series of Mesozoic displacements (Williams et al., 2016), with the OMF and IMF having dominantly north west and north east structural trends, respectively. The Captain Sandstone is bound, at its most northerly extent, by the Wick Fault Zone, with the Smith Bank, West Halibut and Little Halibut Faults marking the Halibut Horst, a Jurassic structural high to the north of the storage site. The Halibut Horst influenced the deposition of the Captain Sandstone and other deep submarine fans in the region throughout the Lower Cretaceous, and was eventually submerged in the Late Cretaceous (Ahmadi et al., 2003).

The paleotectonic stresses experienced throughout the region include a major rifting episode that occurred during the Late Jurassic to Early Cretaceous, manifesting as interspersed periods of faulting and quiescence, generating various half-graben and synrift deposits (Hillis et al., 1994; Zanella and Coward, 2003). At this time, the extension direction was NE-SW, which produced NW-trending normal faults and locally reactivated faults (Zanella and Coward, 2003). Post-rift thermal subsidence, evidenced by the onlap of Lower Cretaceous sands and shales on the basin margins and Upper Cretaceous chalks on the basin highs, was set against a background of rising sea level (Hillis et al., 1994), which was interspersed with periods of sea level fall throughout the Lower Cretaceous (Oakman, 2005). Pulses of compression, originating from the Alpine Orogeny, are interpreted to have occurred throughout the Lower Cretaceous but had minimal effect on the study area (Zanella and Coward, 2003). In the Palaeocene, regional uplift of the Scottish Highlands and the East Shetland Platform led to the deposition of siliciclastic sediments, with a shelf-environment prevailing in the study area (Ahmadi et al., 2003; Garrett et al., 2000). Uplift during the Cenozoic occurred, evidenced by Mesozoic and Cenozoic rocks sub-cropping on the sea bed within the Inner Moray Firth, due to reactivation and propagation of earlier faults up to the seabed (Argent et al., 2002; Richardson et al., 2005).

The orientations and magnitudes of the present-day stress-field vary across the North Sea; the Northern North Sea, influenced by stresses associated with the most recent deglaciation, is close to the transition between reverse and strike-slip faulting $\sigma_{Hmax} > \sigma_v \sim \sigma_{hmin}$, where σ_{Hmax} is the maximum horizontal stress; σ_v is the vertical stress; and σ_{hmin} is the minimum horizontal stress (Hillis and Nelson, 2005). The stress regime in the Central North Sea is highly variable, with the sedimentary sequence appearing detached from the basement; within the sedimentary sequence the stress regime is predominantly that of normal faulting, $\sigma_v > \sigma_{Hmax} \sim \sigma_{hmin}$ (Hillis and Nelson, 2005). Within the Southern North Sea a similar variability in stress orientations are attributed to a detachment across a weak horizon, in this case the Zechstein evaporite sequence (Williams et al., 2015).

Further work, specifically within the Cretaceous and younger strata of the Moray Firth, by Williams et al. (2016) investigated the stability of faults in the region in response to varying pore pressures that may result from CO_2 injection. This investigation used hydrocarbon well data, including a variety of hydraulic pressure tests, downhole ultrasonic televiewer and electrical borehole image logs and downhole bulk density logs. They concluded that normal, strike-slip or normal/strike-slip transitional faulting stress regimes might prevail at reservoir depth in the region with a relatively uniform σ_{Hmax} orientation of NNE-SSW. From modelling potential stresses from large-scale CO_2 injection, they suggested that some segments of the regional faults would be critically-stressed under some of the possible stress conditions and would reactivate with only a minor pore pressure increase. However, these critically stressed faults are only present in the most conservative of cases where differential stresses are at their maximum, as such these are an end-member scenario which is quite unlikely to occur. Also, it is likely that smaller, local, faults would reactivate first thus mitigating stress changes upon the larger regional faults and if faults do reactivate beyond the CO_2 plume footprint, then formation water rather than CO_2 would leak from the storage site thus relieving some of the fluid pressure (Hannis et al., 2013). Specifically, the Acorn CO_2 Storage Site has no major faults occurring within close vicinity to the injection site aside from the West Halibut Fault to the north which is not critically stressed. Other major faults in the region occur at minimum 30 km to the north west, far from the proposed injection site (Williams et al., 2016).

1.2. Site history

1.2.1. Petroleum exploration

The Captain Sandstone has undergone substantial petroleum exploration with a number of oil and gas producing fields, including: the Atlantic, Blake, Captain, Cromarty, Golden Eagle, Goldeneye and Hannay fields, all of which are top-sealed by the shales of the Carrack and Rodby Formations (Pinnock et al., 2003). Within the Acorn CO_2 Storage Site itself, i.e. the Captain Sandstone Fairway, the Atlantic (condensate) and Cromarty (gas) fields have recently been decommissioned while the Blake (oil) field is expected to cease production in 2026. Hydrocarbon plays beneath the Captain Sandstone include the Upper Jurassic Solitaire (gas and oil) and Ross (oil) fields, both of which

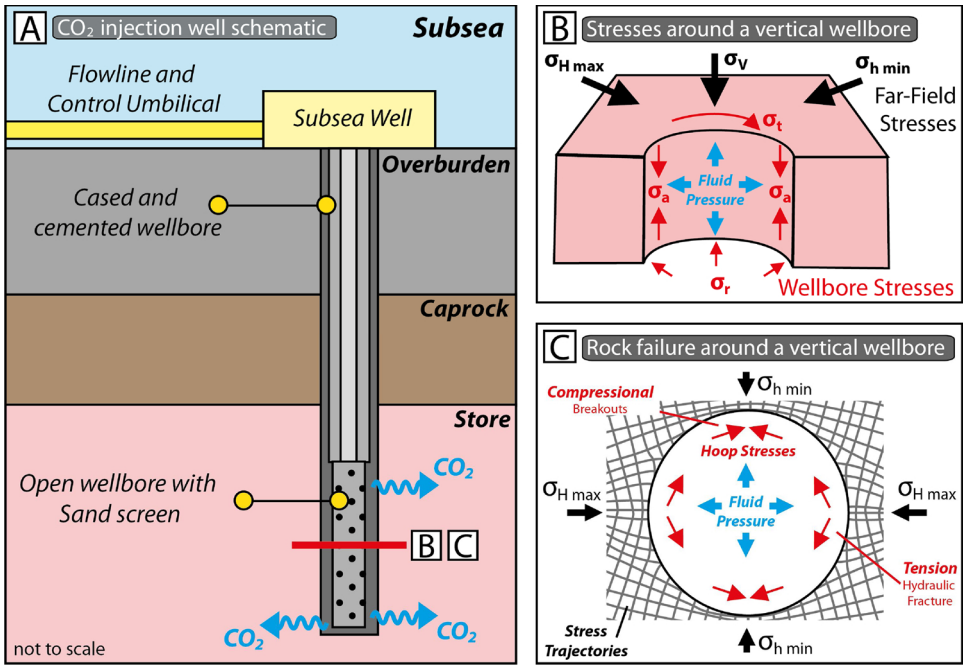

Fig. 2. [A] A schematic illustration of the CO_2 injection well. [B] Stresses around the wellbore. The far-field stresses or formation stresses are represented by σ_v – vertical, σ_{hmin} – minimum horizontal, and σ_{Hmax} – maximum horizontal stresses. The wellbore stresses are represented by σ_a – axial, σ_r – radial and σ_t – tangential/hoop stresses. Modified after Bratton et al. (2004). [C] A schematic illustration of the stresses experienced in the near wellbore rock where; [C] Depicts principal stress trajectories around a cylindrical opening in a bi-axial stress field based on the Kirsch equations (Kirsch, 1898), modified after Zoback (2007). Note that as the wellbore wall is a free surface, the principal stress trajectories are parallel and perpendicular to it.

are currently undergoing production. Neither of these fields are considered to be hydraulically connected to the Captain Sandstone; the Ross Field, in fact, contains no wells that penetrate the Captain Sandstone.

1.2.2. Previous CCS studies on the Captain Sandstone

The Captain Sandstone has been considered for CO_2 storage by several projects in the past, primarily focused on determining suitable locations within the Captain Sandstone for operations to take place. The first was the 2011 Goldeneye FEED Project, which was part of the UK Government's first CCS competition, that aimed to inject CO_2 from the Longannet Power Station into the Goldeneye Field via its existing production platform (ScottishPower CCS Consortium, 2010). The 2015 CO_2 Multistore Joint Industry Platform, envisaged 360 million tonnes of CO_2 captured and injected over a 35 year timeframe via two injection sites (Scottish Carbon Capture and Storage et al., 2015). The 2015 Goldeneye FEED project had similar aims to the previous FEED project except with CO_2 sourced from the Peterhead Power Station and it being part of the UK Government's CCS Commercialisation Programme (Shell, 2015a). The 2016 Strategic UK CO_2 Storage Appraisal Project (ETI SSAP), funded by the Energy Technologies Institute, produced a portfolio of five CO_2 storage sites, one of which was within the boundaries of the Acorn CO_2 Storage Site, with storage development plans and budgets for each site (Pale Blue Dot Energy and Axis Well Technology, 2016a). Other CCS related research on the Captain Sandstone include: the Williams et al. (2016) study, as detailed above, on stress fluctuation and fault reactivation; the Jin et al. (2012) study, which evaluated the CO_2 storage capacity of the Captain Sandstone; and the McDermott et al. (2016) study, which performed a numerical assessment on the geomechanical (mechanical and thermal) stability of the Captain Sandstone as a shared-user CO_2 storage site.

Work presented by Guariguata-Rojas and Underhill (2017) raised concerns regarding the injection of CO_2 into the north western region of the Captain Sandstone. They suggested that CO_2 injected in this region could result in leakage at the seabed through migration of CO_2 up dip towards the Captain Sandstone's western seabed subcrop, as well as via a number of throughgoing faults. In light of this, reservoir simulation of the proposed Acorn CO_2 Storage Site, reported in Pale Blue Dot Energy (2018a), which is situated at the deeper extent of the reservoir to the south east (see Fig. 1), showed that of the proposed 152 MT of CO_2 after 1000 years post-injection: 13 % is structurally trapped; 35 % is residually trapped; 33 % is dissolved in oil/water; and 20 % continues to be mobile at less than 10 m/year, within the bounds of the storage site. These models indicate safe CO_2 storage within the Acorn CO_2 storage site boundary for a minimum of 1000 years away from faulting and seabed sub-cropping to the north west.

2. Reservoir geomechanics

For any geomechanical analysis, the in situ stress conditions are compared with those required to promote rock failure. Here the basic principles of determining the in situ stress, and also laboratory testing to determine rock strength, are introduced.

2.1. Wellbore stresses, their fluctuation and determination

During the injection of fluids into a well, failure of the wellbore surface by tensile fracturing can be induced when fluid pressures exceed the rock tensile strength plus the local minimum principal stress. This hydraulic fracturing process can be purposely induced to increase the transmissibility of rock, when used with proppants, for hydrocarbon extraction (shale gas) and geothermal fluids. However, these tensile fractures can result in a modification of the reservoir unit surrounding the wellbore which may hamper long term fluid injection and borehole integrity. Conversely, during extraction from a reservoir, stresses may increase around a wellbore, potentially leading to compressive failure, borehole breakouts, and wellbore failure.

The far-field stresses acting in a region, the vertical stress (σ_v) and minimum and the maximum horizontal stresses (σ_{hmin} and σ_{Hmax}), are modified once a void, or borehole, is introduced into the subsurface. The modified stresses close to the wellbore can be predicted and described using a polar coordinate frame as the axial stress σ_a, the radial stress, σ_r and the tangential or hoop stress σ_t. These concepts are illustrated in Fig. 2.

The penetration of a vertical well into the subsurface causes the far-field stress trajectories to bend both parallel and perpendicular to the wellbore (Fig. 2C). This is due to the wellbore wall being a free surface which cannot support shear traction. These stress trajectories can be described by Kirsch equations (Jaeger et al., 2007; Kirsch, 1898); where the trajectories of maximum compressive stress converge, stresses are

more compressive in the case of a vertical well (at the azimuth of the minimum horizontal stress; σ_{hmin}). Where the trajectories diverge, the stresses are less compressive (at the azimuth of maximum horizontal stress; σ_{Hmax}). When compressive stresses on the wellbore surface exceed the rocks strength, then breakouts occur; once formed, breakouts increase in depth but not width (Haimson and Herrick, 1986; Zoback et al., 1985), resulting in disaggregation of the wellbore and sand production. Hydraulic fracturing occurs when tensile stresses exceed yield on the wellbore.

The determination of pressure and stress conditions within a subsurface reservoir and the wellbore can be determined directly during operations through a number of techniques and tools. The vertical stress within a reservoir can be measured through integration of the downhole bulk density logs as a function of depth from the surface to the depth of interest, corrected for water depth when in an offshore setting, and assuming isotropic conditions in a horizontal plane (Zoback et al., 2003). Determination of the minimum horizontal principal stress, or the minimum fracture pressure, is primarily achieved through leak-off tests (LOT) or mini-frac tests, where the well is shut in and the wellbore pressurised until fracturing occurs. If this imparted pressure does not exceed the minimum principal stress then a formation integrity test, bleed off test or limit test (FIT, BOT or LT) has been performed, giving a minimum estimate of the minimum principal stress (Zoback, 2007). The maximum principal stress cannot be measured directly so it must be determined through a combination of drilling-induced tensile fractures, or breakouts along the wellbore surface observations, σ_{hmin} measurements, and rock strength (Barton et al., 1988). Observations of the wellbore are performed using downhole ultrasonic televiewers and electrical borehole image logs and also give information on σ_{hmin} and σ_{Hmax} orientation (Zoback et al., 1985).

2.2. Determining the yield state and its evolution of porous rock

A reduction of total porosity within siliciclastic sediments can have a great impact on fluid flow, primarily due to loss of interconnected pore spaces, resulting in permeability reduction. A reduction of connected porosity, i.e., the void space, between clastic grains, can be can be achieved by mechanical or chemical compaction. During the initial burial of a sediment, compaction is largely controlled by mechanical processes such as grain rearrangement, grain crushing and localized faulting (Aydin and Johnson, 1978; Fisher et al., 1999). With increasing burial depth ($>$ 2000 m and $>$ 80 °C), as temperatures and pressures increase, chemical compaction begins to dominate, by pressure solution and cementation, further reducing primary porosity (Worden and Burley, 2003).

Within relatively shallow hydrocarbon reservoirs and aquifers, along with the relatively short timescales associated with injection or production, mechanical deformation is most relevant. Constraining the nature of mechanical deformation in porous rock is key for understanding a range of geotechnical problems including: borehole stability (Cuss et al., 2003a, 2003b; Dresen et al., 2010), reservoir subsidence and compaction (Fisher et al., 1999; Makowitz and Milliken, 2003; Nagel, 2001), and the creation of deformation bands and faulting (Antonellini et al., 1994; Aydin and Johnson, 1978; Ballas et al., 2013; Griffiths et al., 2018).

The onset of mechanical deformation in porous rock is typically defined using a yield curve plotted in P – Q space, where;

$$\text{P is the effective mean stress: } \left(P = \frac{\sigma_1 + \sigma_2 + \sigma_3}{3} - P_f\right) \quad (1)$$

$$\text{Q is the differential stress: } (Q = \sigma_1 - \sigma_3), \quad (2)$$

with σ_1, σ_2 and σ_3 being the principal stresses and P_f being the pore fluid pressure; see Fig. 3B for an illustration of this concept. The yield curve separates regions of recoverable, or elastic, deformation from regions of permanent, or inelastic deformation. At the onset of yield, the response of the rock can be broadly separated into two regimes: dilatational or compactional. At low effective pressures, or low porosity, inelastic deformation is associated with dilatancy and localised faulting (Menéndez et al., 1996), while at higher effective pressures or high porosity, deformation transitions to cataclastic flow and distributed compaction (Bedford et al., 2019; Curran and Carroll, 2018; Wong and Baud, 2012). The two regimes are separated by the critical state point, where constant volume deformation will occur on yield.

During elastic deformation, when stresses sit below the yield curve, poroelastic behaviour can be predicted using elasticity theory. It is possible to map the evolution of the strength and properties of porous rock as stresses reach and then exceed yield, and permanent deformation accumulates (Cuss et al., 2003b; Rutter and Glover, 2012). The initial yield curve characterization has traditionally been derived from axisymmetric triaxial compression tests ($\sigma_1 > \sigma_2 = \sigma_3$), where several specimens of a given rock type are axially loaded under a range of effective pressures until inelastic deformation begins, e.g., see Fig. 3A (Wong et al., 1997; etc.). Note that yield of porous rocks can be reached purely by hydrostatic stresses. This is the point where the yield curve intersects the P-axis and is known as P*, see Fig. 3. Pore-collapse and grain-crushing initiate at P* (Zhang et al., 1990).

During deformation, porosity will increase or decrease because of either compaction or dilation, causing the yield curve to either expand in the case of compactive failure, or contract in the case of dilatancy. A family of yield curves can be produced that illustrate the change in yield strength and deformation regime with changing stress conditions once the specimen has yielded. The critical state points for each of these curves can be joined to form the critical state line (CSL), which separates dilatational and compactional deformation regimes (Fig. 3A and B).

In previous investigations, multiple samples have been used to map out the yield surface, each taken beyond yield at different points around the yield curve (e.g. Baud et al., 2006). However, this method results in data scatter due to inevitable heterogeneity between natural samples. In order to avoid the heterogeneity between samples, this study has used a novel variation on the technique, first detailed by Bedford et al. (2019, 2018) whereby a single sample, from each respective well or depth, is used to determine the yield surface. This approach reduces the amount of scatter due to natural heterogeneity and reveals a high-resolution view of the yield surface. It is also advantageous when material for sample preparation is limited, such as with recovered core samples. Lithologies tested using variations of this yield curve method include: sandstones (Baud et al., 2006, 2004, 2000b; Cuss et al., 2003a, 2003b; Louis et al., 2009; Wong et al., 1997); limestones (Baud et al., 2009, 2000a; Cilona et al., 2014; Veronika et al., 2004); volcanic rocks (Wei et al., 2011); dehydrated serpentinite (Rutter et al., 2009); and bassanite (Bedford et al., 2018).

3. Methods

The following section outlines the sampling strategy of the materials detailed in this study; the geomechanical testing techniques and equipment, including splitting tensile strength and yield curve tests; the petrographic analyses, including optical microscopy, quantitative evaluation of minerals by scanning electron microscopy (SEM-EDS), X-ray diffraction analyses (XRD) and mercury intrusion porosimetry (MIP).

3.1. Sampling, cored-wells and geographic distribution

The materials analysed throughout this study were acquired from multiple, historic petroleum exploration and appraisal wells in North Sea prospects, wells: 13/30-3 (operated by Repsol Sinopec Resources UK Ltd), 14/26-1, 14/26a-6, 14/26a-7A and 14/26a-8 (operated by CNOOC-Nexen Petroleum UK Ltd). These wells were shortlisted due to their occurrence within the proposed Acorn CO_2 Storage Site, their proximity to the proposed primary CO_2 injection sites, the presence of core within relevant reservoir and caprock lithologies and their

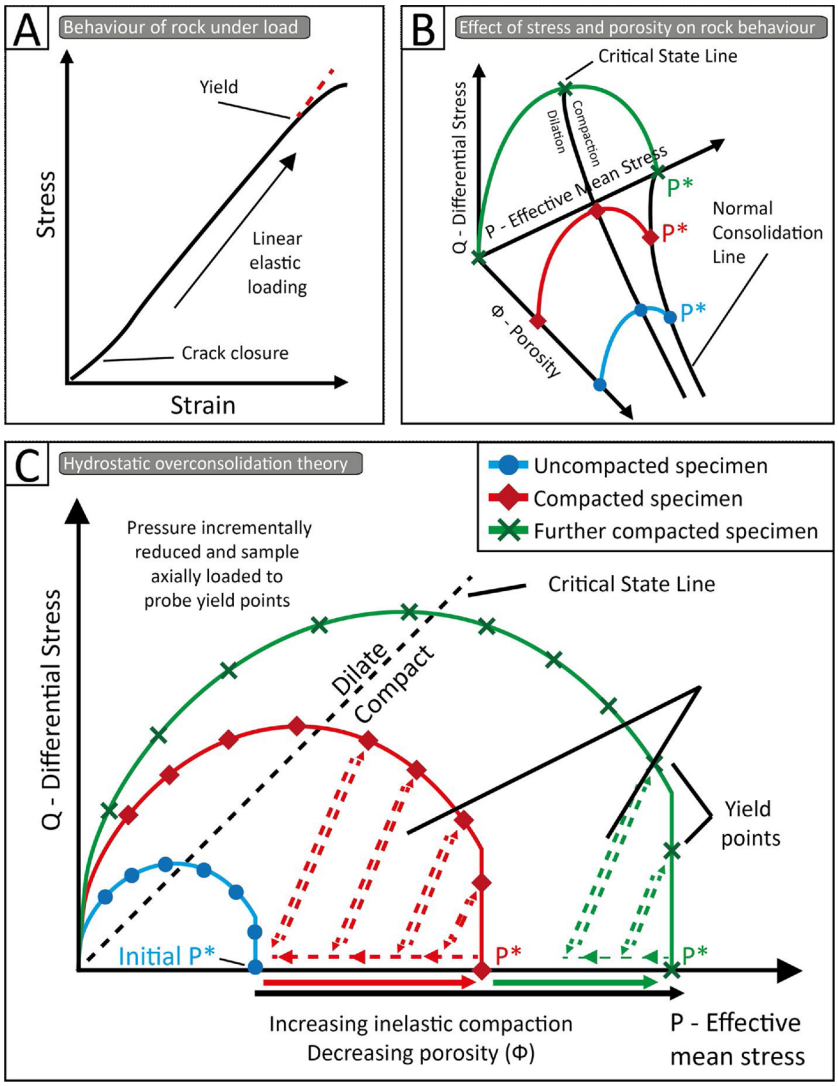

Fig. 3. A schematic illustration and summary of the yield curve technique from Bedford et al. (2018) which shows: [A] As a rock is put under load, its initial response is elastic (i.e., the strain is recoverable). If the load is increased further, then the rock will eventually move out of the elastic regime and begin to accumulate permanent inelastic strain. The stress at which the onset of inelastic strain occurs is called the yield point and can be identified by the deviation from linear elastic loading. [C] For porous rock, a curve can be defined in P – Q space (effective mean stress vs. differential stress) to define the locus of points where yield occurs. This curve is broadly elliptical in shape and can be separated into two regimes. At low effective pressure (P), the mode of deformation is dilatancy and localisation. At high effective pressure (P) the rock will experience distributed, shear-enhanced compaction. Once a porous rock has yielded, its porosity will either increase or decrease depending on which side of the yield curve the stress path intersects. The rock will now sit on a new yield curve because of the change in porosity. These subsequent yield curves can be defined and the Critical State Line (CSL), which separates regions of compaction from dilation, is drawn by joining the crests of the ellipses. During the experiment, the test specimen is hydrostatically loaded so that inelastic volumetric strain is accumulated and permanent compaction occurs (P*). The pressure is then incrementally reduced, to move back inside this new curve and the test specimen subjected to elastic axial loading between each pressure reduction step. The axial load is applied until the deviation from linear elastic loading is observed (A) upon which it is immediately removed. Once the yield curve is fully probed, the sample is further overconsolidated so that more inelastic volumetric strain is accumulated and compaction occurs. The subsequent yield curve is then probed in the same way to determine if there is any shape evolution. [B] A 3D representation of the yield envelope where the third axis is porosity (Φ). The yield curves space out along the porosity axis and their respective P* points are joined by the Normal Consolidation Line (NCL).

availability for sampling (Pale Blue Dot Energy, 2018a). The geographic location of the sampled wells in the Acorn CO_2 Storage Site, are shown in Fig. 1 and Appendix A Table A1.

In order to get a representative data set from the storage site lithologies, the cored depth intervals selected for subsampling were chosen to systematically cover the key variables in the lithologies, including: availability of core, depth, occurrence relative to gas/oil/water-contacts; core porosity, and general lithological variation, as determined from hand specimen (i.e. core) observations, gamma ray and density wireline logs. The sampling of the five wells for this study is illustrated in Fig. 4. All depths reported in this study are core depths, unless otherwise stated.

3.2. Petrographic characterisation of reservoir and caprock samples

Characterisation of the petrographic properties of both the reservoir and caprock specimens used in the geomechanical tests, both pre- and post-test, was undertaken to determine the geo-material controls on rock strength and ultimately to upscale these findings throughout the Acorn CO_2 Storage Site.

Sampling for the petrographic analysis portion of this study involved reviewing wireline data, primarily gamma ray and density logs, from cored intervals that were made available for sampling by CNOOC-Nexen Petroleum UK Ltd (14/26-1, 14/26a-6, 14/26a-7A and 14/26a-8) and Repsol Sinopec Resources UK Limited (13/30-3). Intervals of core that were representative of the overall character of the Captain Sandstone reservoir, the Rodby Shale caprock, and the Sola Shale mid-store baffle, were systematically sampled, as well as regions of core that were lithologically atypical i.e. calcite-cemented nodules, for sample preparation into rock billets, which were then shipped for thin section preparation at ALS Petrophysics Ltd. Polished thin sections were prepared in the standard manner to a thickness of 30 µm for rock samples that were first injected with blue dyed resin to highlight any porosity. These thin sections were then used in both optical microscope and Scanning Electron Microscope (SEM) analyses. X-ray diffraction (XRD) was also performed on the Rodby Shale to quantify fine-grained clay mineral type and proportions (Hillier, 2009). Sampling for geomechanical testing involved the selection of specimens that were representative of the overall character of the Captain Sandstone, the Rodby Shale and Sola Shale.

Optical microscopy observations, in both plane polarised (PPL) and cross-polarised (XPL) light, were performed using an Olympus BX51 microscope with an Olympus SC50 camera at x4 and x10 magnifications. Quantitative evaluation of minerals by scanning electron microscopy (QEMSCAN) was performed, which consists of an automated, spatially-resolved petrography system, based within a scanning electron microscope, using energy-dispersive X-ray spectroscopy detectors and an extensive mineral database (Armitage et al., 2010; Pirrie et al., 2004). These analyses give quantitative mineral proportions, grain and pore space morphology and distribution down to 1 µm resolution. This technique was developed by FEI (Field Electron and Ion

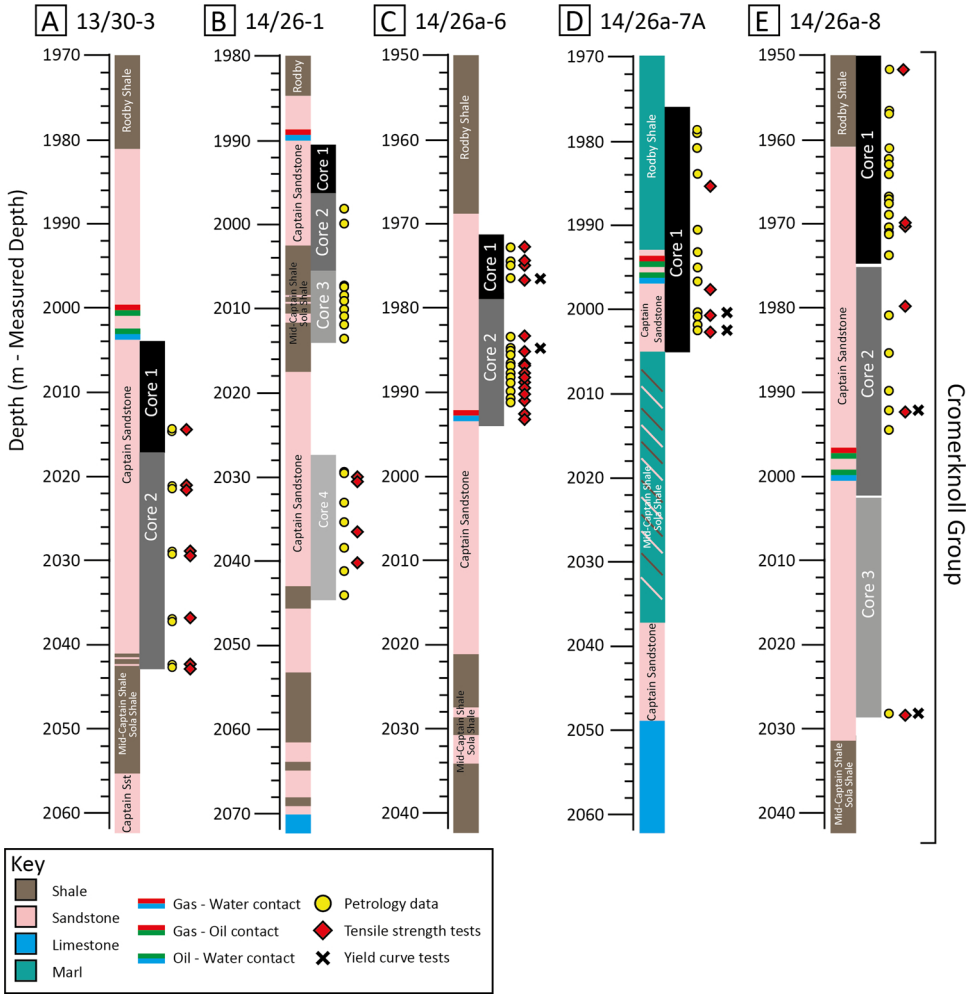

Fig. 4. Summary illustrations of the wells and core sampled in this study and the analyses performed.

Company). Automated SEM-EDS (Scanning Electron Microscope – Energy Dispersive Spectroscopy) is the generic term for this technique. The instrument used in this study is an FEI WellSite QEMSCAN, using a tungsten-filament, operating at 15 kV, equipped with two Bruker EDS detectors (Wooldridge et al., 2018). This technique allowed the microstructural and mineralogical characterisation of the Captain Sandstone reservoir and Rodby Shale caprock. For the purposes of this study, full thin section scans, at a resolution of 20 µm, were performed for quantitative mineralogical proportions, while partial (4.5 × 3 mm) thin sections scans at a higher resolution of 2 µm were performed for more targeted textural/microstructural analysis.

X-ray Diffraction (XRD) analysis was required to quantify the clay mineral proportion of the Rodby Shale caprock and the Sola Shale. Representative sub-samples of the shale were crushed, in distilled water, to a powder < 10 µm using an agate McCrone micronizing mill and dried at 60 °C. Dried samples were then crushed into a light and loose powder in an agate pestle and mortar and back-loaded into cavity holders as random powders. The samples were then saturated with ethylene glycol, by the vapour pressure method at 60 °C for 24 h for accurate determination of the presence of swelling clay (smectite) and its composition. A copper X-ray tube was used, with a nickel filter to select for copper k-α radiation. Scans covered the range of 4–70 ° 2θ. Operation of XRD equipment and software was at the University of Liverpool, using the" HighScore Plus®" analysis software, with quantification achieved using the Relative Intensity Ratio (RIR) method, (Hillier, 2000). Reference patterns for the analysis were acquired from the International Centre for Diffraction Data, Powder Diffraction File-2 Release 2008.

In order to characterise the porosity, permeability, pore dimensions, tortuosity and bulk density of the shale lithologies, mercury injection porosimetry was undertaken; these analyses were performed by MCA Services. Specimens were dried and vacuum outgassed at 60 °C for 24 h. Measurements were made under the assumption that the surface tension of mercury is 0.48 N/m and that the contact angle between specimen surface and mercury is 141 ° (Heling, 1970).

3.3. Geomechanical techniques and experimental procedure

3.3.1. Splitting tensile strength tests

The indirect (Brazilian) tensile testing of rock cores was accomplished by applying diametric compressive stresses on two opposing curved surfaces of a rock disc, (ASTM D3967-16, 2016). This generated a uniform tensile stress on the plane containing the axis of the disc and the loaded surfaces, producing Mode I tensile fractures through the test specimen.

The tests detailed in this study were conducted using a uniaxial press in a Brazilian test jig. The specimen (within the test jig) was compressed unconfined ($\sigma_2 = \sigma_3 = 0$) between a fixed plate and hydraulic piston at a constant loading rate and at room temperature. The applied load was measured using a load cell (Tedea-Huntleigh compression load cell, model 220, grade C4), the load signal was fed through a National Instruments USB-6210 (analogue to digital convertor) device to a computer where the load signal was recorded using LabVIEW software. These tests were undertaken according to ASTM D3967-16 (2016) standards.

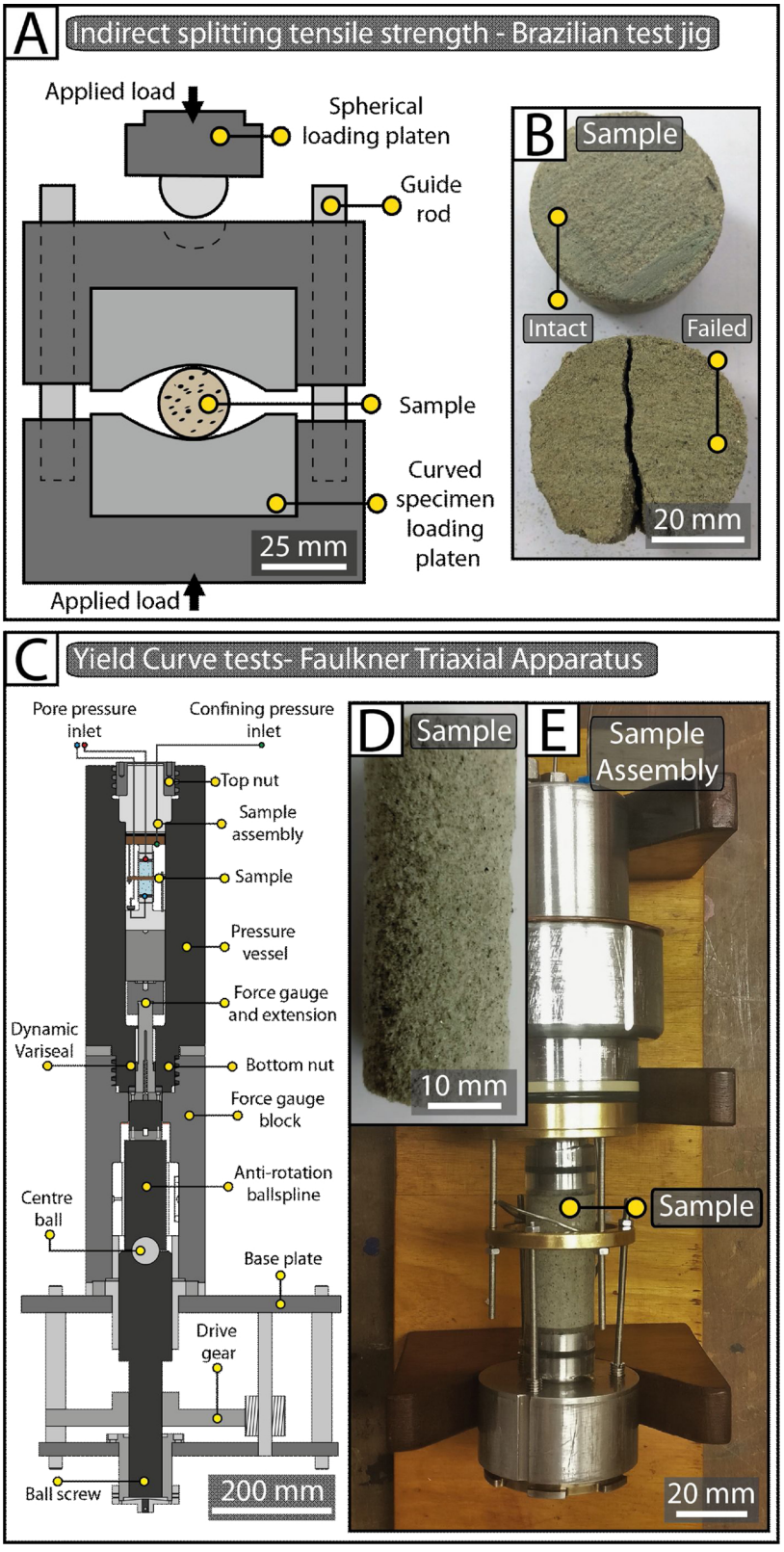

Fig. 5. Experimental geomechanical testing equipment. [A] Schematic of the Brazilian test Jig used for Indirect splitting tensile strength tests. [B] An example of Captain Sandstone test samples before (intact) and after (failed) tensile strength testing. [C] Schematic cross-section of the Faulkner Triaxial Experimental Apparatus used in the yield curve tests. [D] Captain Sandstone test specimen shaped into a 50 × 20 mm cylinder. [E] The sample assembly used to house the test specimen during the experiment.

The Brazilian Test Jig comprised of two blocks of mild steel that house curved bearing platens (D2 steel, hardened to HRC 60). This curvature reduced contact stresses on the specimen. The top block contained a hemispherical seat that housed a chrome ball upon which sat a bearing block; this configuration prevented asymmetric loading once in contact with the uniaxial press's upper fixed plate, see Fig. 5A for experimental set up. Test specimens were comprised of 18 to 38 mm diameter discs with thickness-to-diameter ratios between 0.5 to 0.9,

sampled from half core pieces of the Captain Sandstone reservoir and Rodby Shale caprock.

The larger diameter specimens were used for the most friable material to increase the accuracy of measurement of failure on the load cell, because for smaller specimen diameters failure typically occurred close to the measurement resolution of the load cell (± 20 N). The tensile strengths of these larger diameter specimens had a close correspondence to that of the smaller specimen diameters, once calculated using Eq. (3); the use of larger samples served to validate the measurements performed on smaller diameter specimens.

The calculation of the splitting tensile strength of the test specimen was achieved through the following equation:

$$\sigma_t = 1.272\,P / \pi\,L\,D \quad (3)$$

where σ_t is the splitting tensile strength (STS) in Megapascal (MPa), P is the maximum force applied indicated by the load cell in Newtons (N), L is the length of the specimen in millimetres (mm) and D is the diameter of the specimen in millimetres (mm) (ASTM D3967-16, 2016).

3.3.2. Yield curve tests

The yield curve tests were undertaken to characterise the pre- and post-yield evolution of the Captain Sandstone, where yield is defined as deviation from elastic behaviour and the onset of permanent, inelastic deformation. First, for each sandstone specimen, hydrostatic yield (P*) was determined, where the sandstone was incrementally-loaded hydrostatically until deviation from the elastic, quasi-linear loading path was recognized. Once P* was established, the rest of the yield curve was probed by reducing the hydrostatic load, then axially loading the sample at a rate of 1 μm/s until yield was recognized. Once yield was confirmed, the axial load was unloaded at a rate of 10 μm/s. The effective pressure was then incrementally decreased again and the sandstone was axially loaded until yield at lower effective pressure conditions was reached. This procedure was repeated several times to define the yield curve (Bedford et al., 2018). Fig. 5B provides an illustration of this process.

Once the initial yield curve was mapped, the sandstone was then overconsolidated by hydrostatically loading it above P* after which a new yield curve was established for a permanently, inelastically deformed rock.

The Faulkner triaxial experimental apparatus, used to undertake the yield curve tests, was designed and constructed at the University of Liverpool (Faulkner and Armitage, 2013). This apparatus is capable of triaxial deformation under confining pressures up to 250 MPa, applied using silicon oil confining medium, pore fluid pressures up to 200 MPa and differential loads up to 300 kN. These systems are all servo-controlled, with the confining and pore fluid pressure controlled and measured to a resolution < 0.1 mm^3. The servo-controlled pore fluid system can also be used as a volumometer, allowing the monitoring of changes in pore volume to a resolution of < 0.1 mm^3. De-ionised water was used as the pore fluid in this study, and was held at a constant 20 MPa in all yield curve tests. The axial load was generated by a servo-controlled electromechanical piston and was monitored by an internal force gauge with a resolution of < 0.03 kN.

As stated above, the formation fluid within the Captain Sandstone aquifer is saline water, the salinity of which varies geographically. Pinnock et al. (2003) estimated that this salinity is, on average, 13,000 ppm total dissolved solids from well 13/22a-12, while measurements from well 13/30a-4 indicate a salinity of 62,730 ppm. This geographic variation is attributed to local variations in diagenesis within the Captain Sandstone by the Energy Technologies Institute Strategic UK CCS Storage Appraisal Project (ETI SSAP) (Pale Blue Dot Energy and Axis Well Technology, 2016b). A best estimate of salinity of 56,600 ppm from well 13/29b-8 was used by the ETI SSAP in its appraisal of the Captain Sandstone for CO_2 storage (Pale Blue Dot Energy and Axis Well Technology, 2016b), this intermediate value was also used by the Acorn CO_2 Storage Site Development Plan (Pale Blue Dot Energy, 2018a). During injection of pure CO_2, evaporative dehydration in the near wellbore environment may occur, resulting in the precipitation of halite within the reservoir pore volume. This process represents real-time diagenetic cementation by halite during gas injection. The ETI SSAP – Captain report speculated that, due to the relatively low salinity of the Captain Sandstone formation water, if salt precipitation was to occur, then < 2 % of the near wellbore pore volume would be occupied by halite (Pale Blue Dot Energy and Axis Well Technology, 2016b). Salt precipitation would reduce total porosity from about 28 % to about 26 %; this would have relatively little overall impact on the reservoir permeability and injectivity of the well. Nevertheless, if salt precipitation was to occur, mitigating steps, such as flushing the near wellbore with fresh water, would dissolve the halite and transport it away from the injection site. In regard to the geomechanical properties of the storage site lithologies, the presence of a saline formation fluid would have minimal effect, however, if saline water evaporation and halite precipitation occurred during injection activities then this real-time diagenetic process would likely result in a strengthening of the rock. This effect has been demonstrated in an experimental study by Huang et al. (2018) in which increasing halite salinity, from 0 to 30 % (approximately 0 to 300,000 ppm), resulted in increased geomechanical strength, attributed to an increase in inter-particle friction due to halite crystallisation within the pore space. With this in mind, the use of de-ionised water in the study may slightly underestimate the geomechanical strength of the Captain Sandstone reservoir lithology.

4. Results

This section outlines the general petrographic character of the Captain Sandstone reservoir, the Rodby Shale caprock and the mid-reservoir Sola Shale, the geomechanical tests on both the reservoir and caprock units, and the application of well logs in determining the overall character of the Acorn CO_2 Storage Site.

4.1. Petrology

4.1.1. Sedimentology and general character of the Captain Sandstone, Sola Shale and Rodby Shale

The Captain Sandstone, the primary storage lithology, occurs as an elongate body of sandstone, lying northwest to southeast along the southern edge of the Halibut Horst, (Fig. 1A and B). The main focus of this report is the Upper Captain Sandstone which will be referred to as the Captain Sandstone here forward. The Captain Sandstone member is predominantly composed of thick-bedded, stacked, and amalgamated fine to medium grained sandstones (Pinnock et al., 2003). In the area of this study, the Captain Sandstone is ~70 – 88 m thick which is locally divided by a shale unit, the Mid-Captain Sola Shale, as observed in well 14/26-1 (Fig. 4). The Captain Sandstone is a largely homogenous sandstone body with minor quantities of carbonate cement identifiable in core, and has high porosity (29 to 36 %) and has few discernible sedimentary structures in core. On its upper boundary the Captain Sandstone transitions into the overlying mudstones of the Rodby Shale, and contains fining upwards sequences and ripple cross-stratified thin beds (Pinnock et al., 2003).

4.1.2. Petrographic characterisation of Captain Sandstone reservoir

Initial characterisation of the Captain Sandstone reservoir was performed using optical microscopy. Micrographs illustrating the microstructural and petrographic character of the sandstone are presented in Fig. 6E. The overall character of the Captain Sandstone is that of a high-porosity sandstone with an average conventional core analysis (CCA) porosity of 27.45 %. The Captain Sandstone is composed of moderately-sorted, sub-angular to sub-rounded quartz grains, with grain sizes of 50 to 500 μm diameter. The Captain Sandstones contains relatively little cement, as seen in Fig. 6E. The Captain Sandstone shows little direct evidence of mechanical compaction, with features such as ductile grain deformation, intergranular microcracks in quartz or

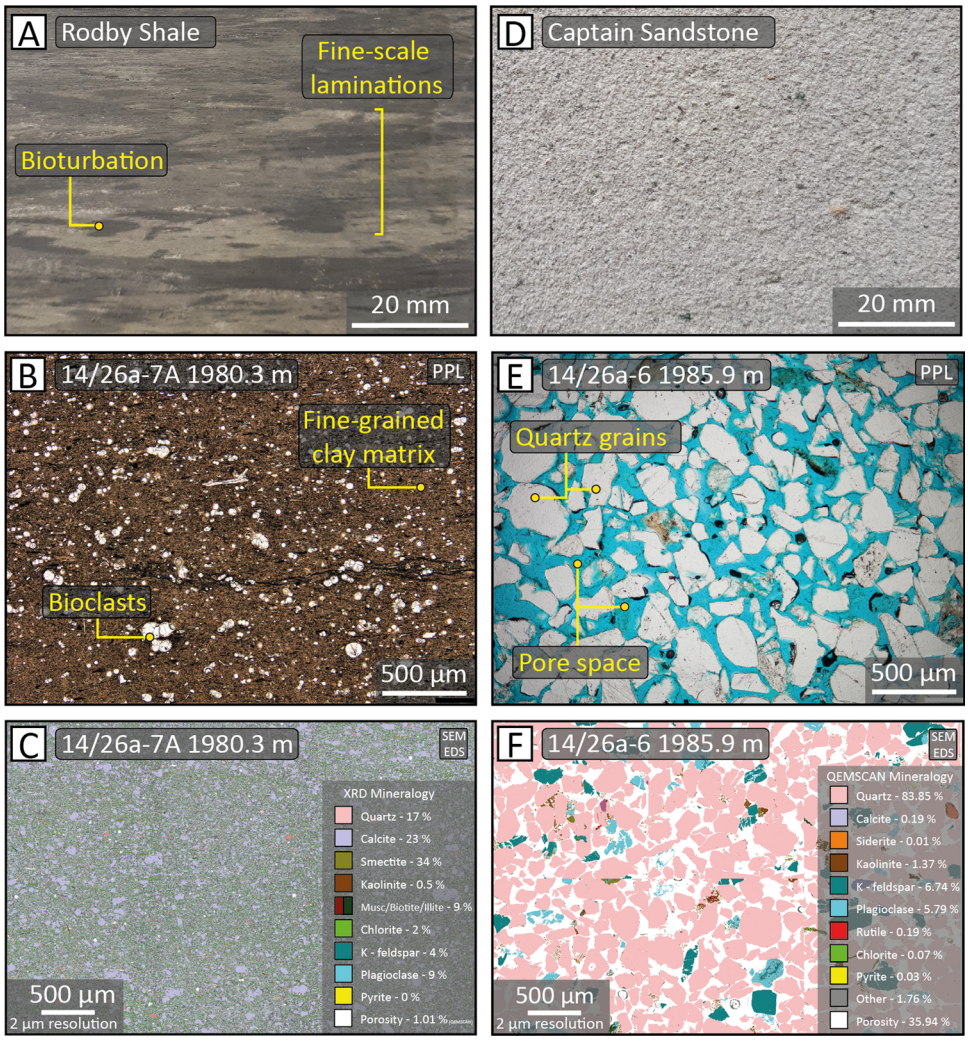

Fig. 6. The petrographic character of the Acorn CO_2 Storage Site lithologies. [A] A hand-specimen image of the Rodby Shale caprock, showing bioturbation and fine-scale laminations. [B] A representative plane-polarised light (PPL) micrograph of the Rodby Shale, showing the fine-grained clay matrix and abundant bioclasts. [C] A Stitched QEMSCAN image showing the mineralogical composition of the Rodby Shale, the mineralogical proportions are taken from XRD analyses. [D] A hand-specimen image of the Captain Sandstone reservoir, showing its largely featureless nature. [E] A representative PPL micrograph of the Captain Sandstone, showing a high porosity, poorly cemented, moderately-sorted, sub-angular to sub-rounded sandstone. Blue colouration is due to dyed epoxy-resin used to impregnate specimens for microstructural analysis, it therefore represents porosity. [F] A Stitched QEMSCAN image showing the mineralogical composition of the Captain Sandstone. For QEMSCAN analyses mineralogical proportions were derived from full thin section scans at 20 µm resolution.

feldspar grains, comminution and cataclastic flow rarely present. Within the Captain Sandstone there exist, as limited horizons, < 3 m thick, calcite-cemented layers, with porosities of 2.7 to 13.9 % (average 5.9 %). These calcite-cemented layers may be laterally continuous as they have been identified in all of the sampled wells at similar depths, however they do not compose a substantial proportion of the rock, and represent a net to gross (i.e. volumetric) consideration rather than a reservoir quality issue.

A representative SEM-EDS image of the Captain Sandstone is shown in Fig. 6F, with quartz (pink), K-feldspar (teal) and plagioclase (blue) grains poorly cemented, and with high remaining porosity (white). Overall SEM-EDS analyses show average mineral proportions for the Captain Sandstone as quartz (81.70 %), plagioclase (5.93 %) and K-feldspar (6.45 %) grains, with minor carbonate (0.64 %) and clay minerals (3.04 %). In two instances (14/26a-8: 1960.90 m and 14/26a-7A: 1996.75 m) plagioclase (~13 %), K-feldspar (~13 %), clay mineral (~5 %)-rich layers occur. Calcite-cemented horizons, on average, are comprised of quartz (57.33 %), plagioclase (4.02 %) and K-feldspar (4.29 %), calcite (29.96 %) and clay minerals (1.61 %).

Tensile strength tests were carried out on both non-cemented, high porosity sandstone and calcite-cemented sandstone; yield curve tests were carried out exclusively on the non-cemented, high-porosity sandstone.

4.1.3. Petrographic characterisation of the Rodby and Sola Shales

The Rodby Shale Caprock is predominately composed of a matrix of very fine-grained clay minerals; XRD analysis of these fine-grained lithologies revealed there was smectite (35.6 %), kaolinite (4.8 %), and chlorite (1.7 %) with some fine-grained quartz (22.1 %), plagioclase (8.6 %) and K-feldspar (5.0 %) grains and calcite occurring as bioclasts (0 to 24.0 %). The Sola Shale is also predominately composed of very fine-grained clay minerals: smectite (26.3 %), kaolinite (10.3 %), and chlorite (3.3 %) with some fine-grained quartz (32.0 %), plagioclase (11.0 %) and K-feldspar (6.7 %) grains. These shales have 500 to 1000 µm (i.e. finely) laminations, with shale horizons interbedded within the Captain Sandstone exhibiting intense bioturbation (Fig. 6A and B) or interbedded layers of fine sand. Bioclasts occur throughout the shale, these are predominantly calcite shell fragments but they do not form coherent layers within the rock. The Mercury injection porosimetry revealed that the shales have an average porosity of 13.75 %, an average permeability of 2.2×10^{-19} m^2 (225 nD) and an average tortuosity of 3320.6.

4.2. Geomechanics

4.2.1. Splitting tensile strength results of the Captain Sandstone, Rodby Shale and Sola Shale

Overall, the tensile strength for the Captain Sandstone is very low. Specimens from the gas/water-legs in the sampled wells range between < 0.1 and 0.74 MPa; oil-saturated specimens range between 0.27 and 0.74 MPa, and calcite-cemented specimens between 3.28 and 4.49 MPa (Fig. 7A). Due to the variability in the experimentally-derived splitting tensile strength values, repeat tests for some depth intervals were performed. Fig. 7B shows a histogram plot of the high porosity Captain Sandstone splitting tensile strengths (STS < 0.74 MPa). The mean is 0.16 ± 0.013 MPa and standard deviation is 0.14 MPa.

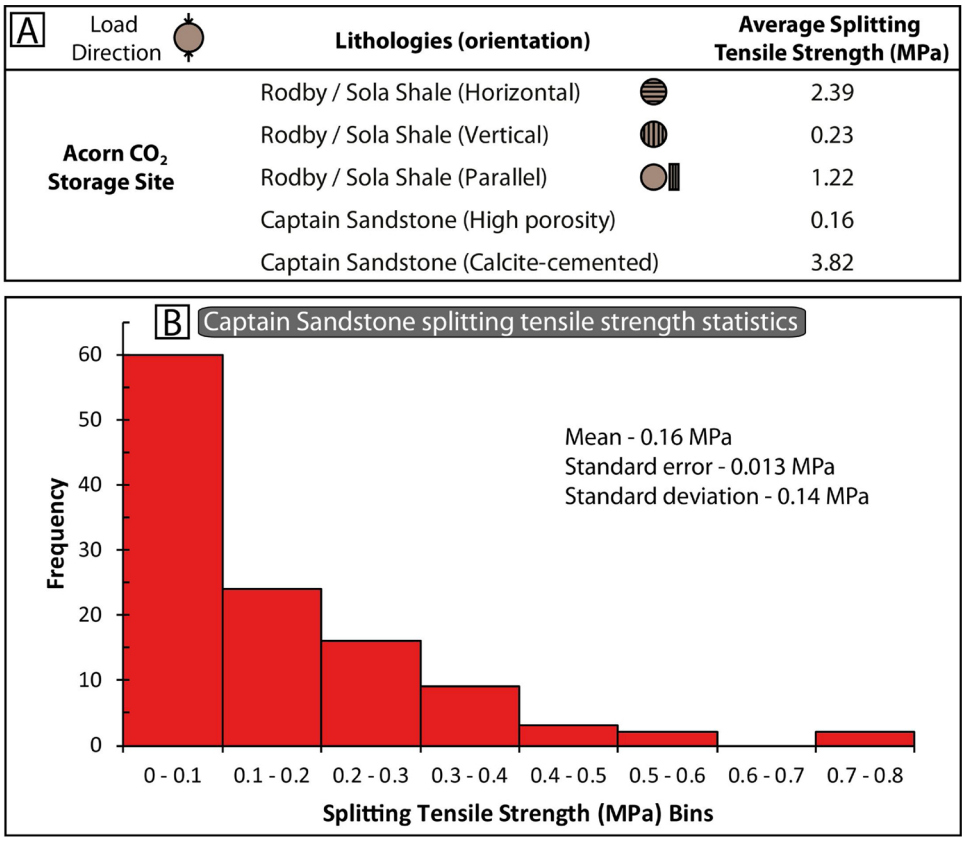

Fig. 7. [A] Splitting tensile strength (STS) values for the Acorn CO_2 Storage Site lithologies. The Rodby / Sola Shale specimens were tested in three orientations relative to their laminations. The Captain Sandstone specimens included both the high porosity, poorly-cemented sandstone that composed most of the member and a number of calcite-cemented intervals for comparison. [B] Statistics of the splitting tensile strength results on the Captain Sandstone.

Appendix B Table A2 shows the full results by well and depth.

In contrast to the largely homogenous Captain Sandstone, the Sola and Rodby Shale contain pervasive laminations on a sub-mm scale. To determine the influence of lamination orientation on the tensile strength of the rock, multiple specimens were prepared from each sampled interval in three orientations, horizontal; vertical and parallel to bedding, as illustrated in Fig. 7A. The average tensile strengths of the Sola and Rodby Shales are: 2.39 MPa at horizontal; 0.23 MPa at vertical and 1.22 MPa at parallel orientations. Note that in Fig. 7A, horizontal, vertical and parallel refer to the orientation of the shale laminations during testing of the specimen and that specimen load direction are indicated by the black arrows.

4.2.2. Captain Sandstone yield curve measurements

The onset of permanent, inelastic compaction (initial hydrostatic yield: P*) for the Captain Sandstone ranges from 78 to 110 MPa effective pressure. The initial P* values for each test specimen are reported in Fig. 8A – F.

Yield curves from of the Captain Sandstone are presented in Fig. 8. Each family of curves represents the conditions at which inelastic yield (i.e. permanent deformation) occurs, when the specimen is axially loaded, at progressively increased hydrostatic pressures and thus progressively reduced porosities. Porosities for each curve are reported with their respective curves; these curves are not strictly iso-porosity contours as elastic unloading of the specimen occurs when the pressure is incrementally reduced during the stress-probing procedure, and this elastic relaxation equates to ~2 % porosity increase.

In each plot of yield curves, the blue curve represents the yield behaviour of the undeformed Captain Sandstone, prior to the onset of P*. In Fig. 8A, B and C for, specimens 14/26a-6 1985.9 m; 14/26a-8 1992.6 m; 14/26a-8 2029.4 m, the red curves show that once P* is exceeded and the sandstone undergoes permanent porosity reduction of 10.4 %, 9.0 % and 7.9 % respectively, its yield curve expands, while being pinned close to the origin. This behaviour is further observed at increased effective pressures and reduced porosity by the green curves.

An additional behaviour has been observed for three samples, illustrated in Fig. 8D, E and F. Specimens 14/26a-6 1977.4 m; 14/26a-7A 2001.1 m; 14/26a-7A 2003.5 m, show that for compaction beyond P* to porosity reductions of 4.2 %, 8.3 % and 7.8 % respectively, the sandstone becomes weaker on the dilatant side of the yield curve. Upon further compaction, at ~40 MPa from initial P*, the sandstone strengthens past the initial yield curve in the compactive region but exhibits a near identical strength in the dilatant region as the original pre-deformed curve (blue).

After the yield curve experiments, the sandstone test specimens were prepared into polished thin sections and analysed using optical microscopy (Fig. 9). In all of the yield curve test specimens, note the reduced porosity, intergranular microfractures and cataclastic flow due to hydrostatic overconsolidation/compaction. Examination of each specimen shows no sample-scale structures or evidence of localisation generated during testing. Deformation appears to have occurred homogenously throughout the sandstone, accommodated by fracturing and cataclastic flow. During cataclastic flow, grains have fractured via intragranular cracking at point contacts (Hertzian fracture) and have then undergone granular flow producing consolidation. This cataclasis and crushing results in a very-fine grained (< 20 μm), poorly sorted deformation product, that fills intergranular pore space and anastomoses around intact relict grains.

4.3. In situ stress and pressure determination within the Acorn CO_2 Storage Site

We collated several well pressure tests for the determination of the minimum principal stresses within the Acorn CO_2 Storage Site. For the wells sampled in this study, a variety of pressure tests were performed during drilling operations: 14/26-1 a Bleed-Off Test (BOT); 13/30-3 a Leak-Off Test (LOT); and 14/26a-7A a Formation Integrity Test (FIT). The data provide constraints on the minimum principal stress in the

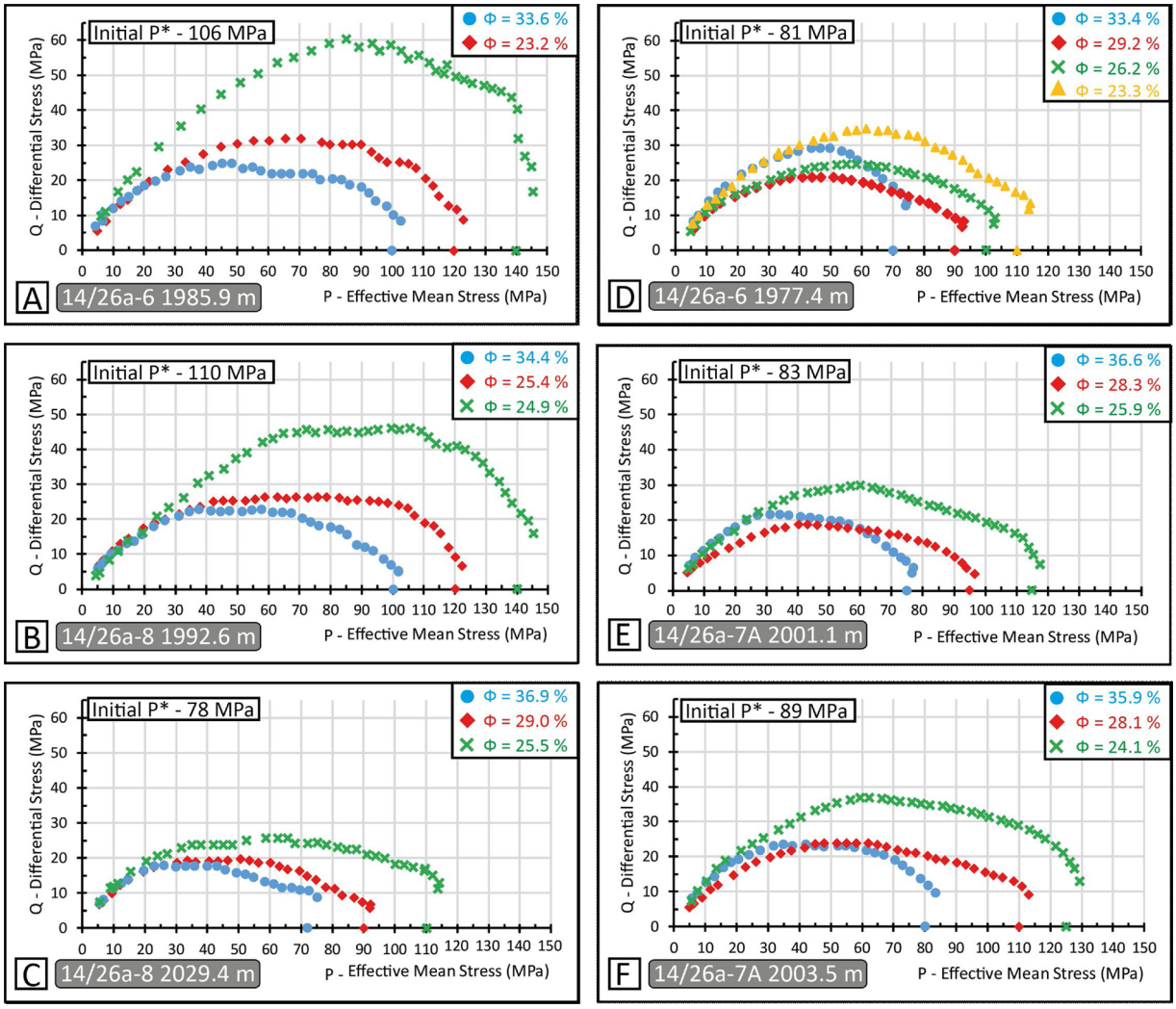

Fig. 8. Plots for the yield curve tests on Captain Sandstone. Blue curves show yield conditions before hydrostatic inelastic compaction (P*), with red, green and yellow curves showing yield behaviour after increased increments of P*. The porosity (Φ) evolution with increasing P* is also shown; where the blue line is the starting porosity; and the red, green and yellow lines show progressively reduced porosity after P*.

region to add to the estimates for in situ stress provided by Williams et al. (2016). If in situ stresses in the reservoir can be determined, they can be compared to the yield envelopes from the mechanical testing to assess how close to failure the reservoir rocks are. The pressure test values were acquired from the well completion reports. Included in the plots of these data are the LOTs for the wells utilised by Williams et al. (2016) for their stress analysis study of the Captain Sandstone, wells: 13/22b-4, 13/22b-19, 13/22b-20 and 13/24b-3. These wells are located ~32 to 34 km to the north west of the wells sampled in this study. Fig. 10 displays the data from the pressure tests.

The pressure tests give a wide range of values, with the 14/26a-7A FIT giving a pressure gradient of 0.0163 MPa/m. Wells 13/22b-4, 13/22b-19 and 13/22b-20, all LOTs, give a pressure gradient of 0.0189 MPa/m. Note that all pressure tests were performed at depths shallower than the Captain Sandstone and Rodby/ Sola Shale. Nonetheless, at a depth of 2000 m, within the Captain Sandstone, this would give σ_{hmin} of 32.58 MPa to 37.82 MPa respectively. Because these pressure tests are not a direct measurement of the minimum principal stress, the gradients shown are an estimate of σ_3 / σ_{hmin} (White et al., 2002; Williams et al., 2016). The estimation of the pore fluid pressure within the Acorn CO_2 Storage Site was undertaken through collation of legacy well report Repeat Formation Tests (RFTs). The results of this estimation are shown in Fig. 10 and have been combined to give a pore fluid pressure gradient of 0.0133 MPa/m.

4.4. Deformation analysis in reservoir space (DARS) analysis

Relating the laboratory-based geomechanical tests and in situ reservoir pressure/stress measurements can be achieved by using a Deformation Analysis in Reservoir Space (DARS) approach. As outlined by Chan and Zoback (2002) and Zoback (2007), DARS aims to integrate laboratory geomechanical data with the physical state of a reservoir in order to predict its evolution through time as pressures/stresses change in response to injection or depletion. The analysis assumes a normal faulting regime, constant vertical stress and no horizontal strain. Thus, the horizontal stresses (σ_{Hmax}, σ_{hmin}) vary according to any change in the pore pressure during injection or depletion.

The result of a modified Deformation Analysis in Reservoir Space analysis for the Acorn CO_2 Storage Site is shown in Fig. 11 for an approximate injection depth of 2000 m. The overburden stress (σ_v) was determined through integration of wireline density logs, the minimum horizontal stress (σ_{hmin}) estimates from LOTs and FITs, and the pore fluid pressure (P_f) estimates from RFTs, performed during well appraisal activities as detailed above. The maximum horizontal stress (σ_{Hmax}) as estimated by Williams et al. (2016) is 50 MPa for a depth of 2000 m in a normal/strike-slip transitional stress regime. Tensile failure, shown as a red yield curve, occurs when the P_f exceeds the combined σ_{hmin} and tensile strength of the rock. Shear failure, shown as the green yield curve, marks the stress conditions in which normal faulting will occur upon pre-existing

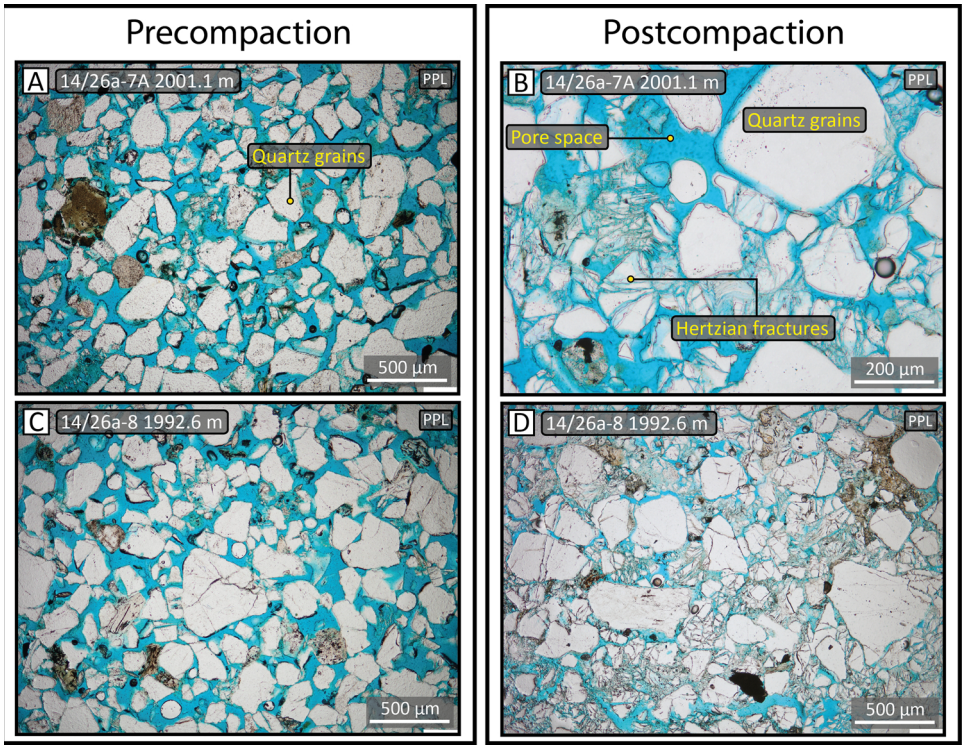

Fig. 9. Optical micrographs of the Captain Sandstone post-yield curve tests and full hydrostatic overconsolidation.

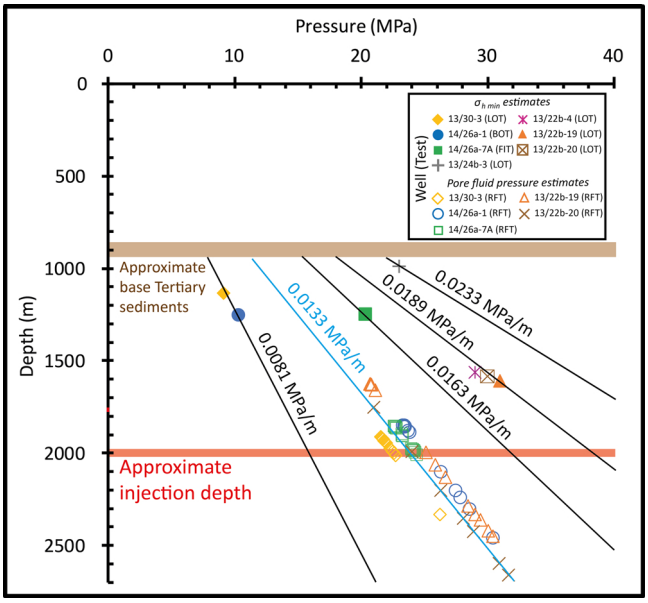

Fig. 10. Pressure test results for wells associated with the Acorn CO_2 Storage Site. Pressure gradients for minimum horizontal stress - σ_{hmin} are marked in black and pore fluid pressure – P_f in blue, with the approximate injection depth, ~2000 m marked. Test acronyms: Bleed-Off Test (BOT); Leak-Off Test (LOT); Formation Integrity Test (FIT); Repeat Formation Test (RFT).

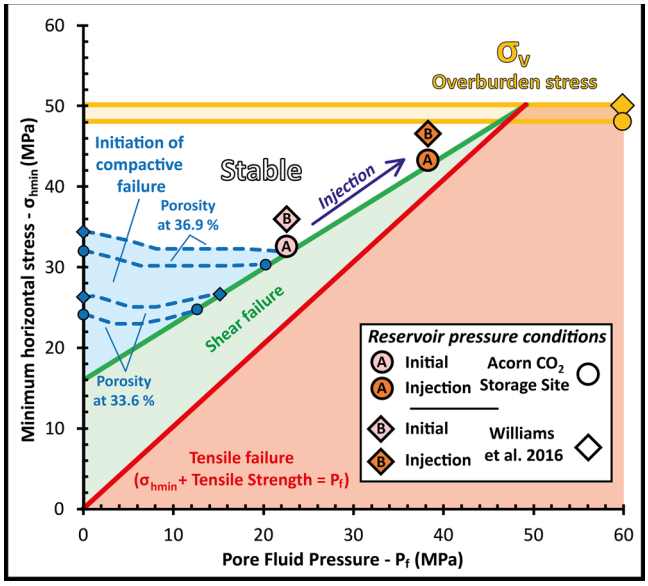

Fig. 11. Deformation analysis in reservoir space (DARS) showing the experimentally-derived yield curves in reservoir space, and the expected stress path around the wellbore, as injection is undertaken. Analysis undertaken at an approximate injection depth of 2000 m. Coloured regions mark pressure/stress conditions in which failure will occur. [A] Pressure estimates using σ_{hmin} values from well 14/26a-7A. [B] Pressure estimates using σ_{hmin} values from wells, 13/24b-3; 13/22b-4; 13/22b-19; 13/22b-20, used in the Williams et al. (2016) study, located ~32 – 34 km north west of the injection site.

faults within the reservoir and corresponds to the Coulomb failure condition; we used a coefficient of friction (μ) of 0.6, a value frequently measured for a wide variety of rocks, including sandstone (Byerlee, 1978; Chan and Zoback, 2002). Compactive failure, shown by the blue window, was determined using the initial, intact yield curves for the Captain Sandstone, detailed in Section 4.2.2., with the yield curves transformed from laboratory P – Q space into reservoir space $\sigma_{hmin} - P_f$ as a function of the principal stresses and pore pressure using the following equations;

$$\sigma_{hmin} = \sigma_v - Q \quad (4)$$

$$P_f = \frac{\sigma_v + \sigma_{hmin} + \sigma_{Hmax}}{3} - P \quad (5)$$

where P_f is the pore pressure; σ_v is the overburden stress; σ_{hmin} is the minimum horizontal stress; σ_{Hmax} is the maximum horizontal stress; P is the experimental effective pressure; Q is the experimental differential

pressure, all in in Megapascal (MPa).

The stress path, how the horizontal stress (σ_{Hor}) changes with varying pore pressure, within the storage site reservoir as injection takes place is defined using the following Eq. (6);

$$\Delta\sigma_{Hor} = \alpha \frac{(1-2\nu)}{(1-\nu)} \Delta P_f \quad (6)$$

Where α is the Biot's coefficient and ν is the Poisson's ratio, this assumes α is constant with respect to changes in pore pressure. If $\nu = 0.25$ and $\alpha = 1$, with a change in pore pressure the horizontal stress should correspond to the following equation (Guéguen and Palciauskas, 1994);

$$\Delta\sigma_{Hor} \sim \frac{2}{3} \Delta P_f \quad (7)$$

The reservoir pressure conditions for two geographic locations within the Captain Sandstone (Acorn CO_2 Storage Site and the Williams et al., 2016 site) have been analysed. As shown in Fig. 11, [A], with circle symbols, average σ_{hmin} estimates from well 14/26a-7A FIT, likely an underestimation due to the limitations of FITs as detailed above in Section 2.1., corresponding to the proposed injection site for the Acorn CO_2 Storage Site. [B], shown in diamond symbols, uses σ_{hmin} estimates from wells, 13/24b-3; 13/22b-4; 13/22b-19; 13/22b-20, from the Williams et al. (2016) study, located ~32 to 34 km north west of the injection site. The pink marker in each setting represents the estimated initial reservoir pressure conditions, with the orange marker representing the change in pressure/stress during injection, for an injection CO_2 pressure increase of 16 MPa, the maximum pipeline delivery pressure at the wellhead. In order to ensure the injection of a single phase liquid, CO_2, through the injection well tubing, a minimum injection pressure of 4.5 MPa must be maintained (Pale Blue Dot Energy, 2018a). For both settings, during the initial injection of CO_2 the stress/pressure conditions within the near wellbore will move towards, but crucially not exceed, the tensile failure yield surface and the overburden stress; this leads us to conclude that the rock in the near wellbore environment should remain intact. It is worth noting that the in situ pressure/stress estimates used in these analyses were performed prior to any petroleum production in the area; in the case of Acorn CO_2 Storage Site, present day pressures/stresses may be less than shown here because hydrocarbon depletion reduces pore fluid pressures. As such, the current stress state of the Captain Sandstone likely means that the estimates shown here are closer to failure than at present within the reservoir.

5. Discussion

This section explores the relationships between the geomechanical properties, petrographic character and wireline log character of the Captain Sandstone reservoir, the Rodby Shale caprock and the mid-reservoir Sola Shale, and how they can be used to characterise the Acorn CO_2 Storage Site.

5.1. Captain Sandstone reservoir geomechanical properties

The direct, experimental measurement of the Captain Sandstone's geomechanical properties has shown that much of the sandstone has a very low tensile strength and, under hydrostatic conditions, undergoes permanent, inelastic compaction at 78to110 MPa, well above the minimum mean stresses derived from LOTs at depths equivalent to the Acorn CO_2 Storage Site. The geomechanical behaviour of the sandstone, once hydrostatic compactive yield is achieved, is variable; some samples show an immediate strengthening, with overconsolidation/porosity reduction, while others undergo an initial post-compaction weakening and then strengthening once hydrostatically overconsolidated by an additional ~20 MPa.

If, during CO_2 injection, the fluid pressures exceeds the minimum principal stress and the tensile strength of the rock, then tensile fracturing (hydraulic fracturing) may occur (Zoback, 2007). This pressure/stress threshold for fracture is known as the formation fracture pressure and may be overcome if the rate of fluid (CO_2) flow into the formation away from the injection site is exceeded by the fluid supply. Such a situation would allow pore fluid pressure to build, resulting in stresses that may deform the rock. The fracture gradient (MPa/m) is the pressure/stress gradient required to fracture the rock at a given depth. It increases with depth due to increasing overburden pressure (Schlumberger, 2018). There is a lack of consensus in the petroleum industry on the calculation of the fracture gradient, with some using the minimum principal stress gradient, and others the maximum leak-off pressure gradient (fracture breakdown pressure gradient), or the fracture initiation pressure gradient (Zhang and Yin, 2017). Knowledge of the tensile strength of the rock in a formation gives us a further constraint on the fracture gradient when used in conjunction with the minimum principal stress and leak off test results.

As detailed above in the DARS analysis, the proposed CO_2 injection pressure of 16 MPa, in addition to the ambient pore pressure of ~22.3 MPa, at 2000 m in the Acorn CO_2 Storage Site, is not sufficient to overcome the minimum horizontal stress (σ_{hmin}) and the overburden stress (σ_v) around the wellbore. Thus, tensile failure of the near wellbore rock is unlikely. However, as outlined in Section 2.1 local stresses around the wellbore will be modified by the free surface of the borehole being unable to support shear traction, resulting in a local decrease in σ_{hmin} and an increase in σ_{Hmax}, which may result in the shear failure of the wellbore even prior to any injection activity. Such an occurrence would become apparent during initial drilling activity and can be mitigated. If the borehole was to remain intact during initial drilling it would remain so throughout injection according to our results.

If, in the event that the injection pressure was to overcome σ_{hmin}, then the very high permeability of the Captain Sandstone, with an average permeability of 2.1×10^{-12} m^2 (2114 mD) from CCA analysis reports, would result in the rapid dissipation of the pressure within the overpressured volume, resulting in a transient effect on the rock structure. Also, as shown in the yield curve results, if stresses do exceed the yield strength of the rock, porosity would be reduced by only 4to10 %, so that reduction of CO_2 injectivity would be minimal.

5.2. Relationship between Captain Sandstone reservoir geomechanical properties and petrographic character

Controls on rock strength for siliciclastic rock, including unconsolidated aggregates, have been attributed to a range of petrographic properties, including: porosity, grain size, mineralogy, cementation and presence of sedimentary structures (Wong et al., 1997; Wong and Baud, 2012; Zhang et al., 1990). Any variation in these properties can have great influence on a rock's mechanical behaviour, with studies performed by Tembe et al. (2008) showing that, for two sandstones of identical grain size and porosity, one with a homogenous mineralogy of quartz had a far greater yield strength, by a factor of two, than one containing 26–30 % feldspars. This same effect applies with the presence of other weak mineral phases such as micas and clay minerals.

The Captain Sandstone has a high porosity (29 to 36 %), is largely devoid of any core-scale sedimentary structures, has little carbonate-cement (0.26 – 0.81 %) other than in limited horizons or nodules, and has a consistently high quartz (75.53 to 89.07 %) and low clay mineral (1.83 to 5.18 %) concentrations. It can be inferred that porosity and grain size play a dominant role in the geomechanical behaviour of the Captain Sandstone. This potential primary control of porosity on strength is illustrated in Fig. 12 which shows a plot of the high porosity, gas/water-leg Captain Sandstone splitting tensile strengths (STS < 0.74 MPa) against porosity. Porosity, and thus the inverse of the degree of compaction and cementation, appears to have a moderate, negative correlation with a reduction in tensile strength. The stronger horizons that exist throughout the sandstone, including calcite-cemented nodules or doggers and oil-saturated sandstones, do not compose a substantial portion of the rock, with only the calcite-cemented doggers

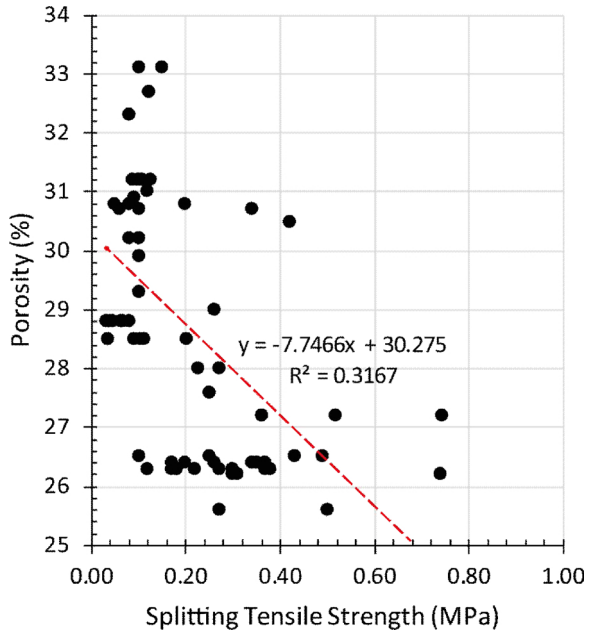

Fig. 12. Cross-plot of the Captain Sandstone splitting tensile strength and porosity.

exhibiting locally decreased porosity. As observed in the compressional sonic and density log wireline data, these horizons represent a net to gross consideration rather than a reservoir quality issue; as such they are unlikely to greatly influence CO_2 injection operations.

The yield curve tests, performed in this study, show that the Captain Sandstone has a relatively high P* in comparison to other high porosity sandstones, such as the Boise and Idaho Gray Sandstones, porosities of 37.6 % and 36.2 % respectively, with yield curve tests on these sandstones giving P* values of 37 to 48 MPa and 54 to 59 MPa (Bedford et al., 2019). The main differentiator for the strength of these high porosity sandstones appears to be mineralogical; the Boise and Idaho Gray sandstones contain a greater proportion of weaker mineral phases, with quartz contents of 46.08 % and 51.93 % respectively, compared to the Captain Sandstone quartz content of 81.70 %. Under hydrostatic pressures the quartz/feldspar grains in poorly cemented sandstones act a framework, with grain-grain contacts; once P*, and thus the strength of the sandstones constitutive minerals, is overcome these grain-grain contacts are destroyed, with the disaggregated grain fragments mobilised into the original pore space of the rock, thus reducing porosity.

A theoretical model, based on Hertzian indentation cracking, on estimating pore collapse (P*) for sandstones has been proposed by Zhang et al. (1990), where the effective hydrostatic pressure required to initiate grain crushing is determined as a product of initial porosity (Φ), as a fraction, and the radius of the individual grains (r) in mm. In this case resulting in a plot of log P* vs log (Φ r) with a slope of -3/2. This model was verified with experimental data on a variety of sandstones from Cuss et al. (2003b); Rutter and Glover (2012) and Wong et al. (1997). P* in MPa can be estimated with the following equation:

$$\log P^* = 0.603 - 1.09 \log(\Phi r) \quad (8)$$

As the Captain Sandstone is friable and poorly cemented, fracturing will likely be accompanied by extensive disaggregation around the wellbore. This disaggregation may hamper injection as porosity and thus permeability may be diminished around the injection depth interval, as loose material accumulates. Therefore, keeping fluid injection pressures below this threshold, i.e. the fracture gradient, is strongly recommended.

Geochemically, the homogenous, quartz-rich mineralogy of the Captain Sandstone is unlikely to undergo much CO_2-rock interaction during injection and storage operations. The minerals most susceptible to alteration, such as plagioclase, K-feldspar, carbonates and clay minerals form a minor proportion of the rock (< 20 % in total) and are evenly disseminated throughout, so that, even if these more reactive minerals dissolved, the overall integrity of the quartz grain-grain framework would be unlikely to be compromised. Additionally, experimental work on the mechanical effect of CO_2 injection on simulated reservoir sands, performed by Hangx et al. (2010), showed that the presence of CO_2 inhibits stress corrosion and microcracking in both quartz and feldspars, due to the acidification of the pore fluid. As such, on the timescales of injection and storage CO_2-rock chemical interactions within the Captain Sandstone reservoir will be negligible and will not hinder CO_2 storage activities.

5.3. Relationship between the Rodby Shale caprock and Sola Shale geomechanical properties and petrographic character

As the Captain Sandstone reservoir is sealed primarily by the overlying Rodby Shale, mitigation of any potential CO_2 leakage through this lithological seal is imperative. Ensuring that the Acorn CO_2 Storage Site's seal integrity is maintained over the period of injection and storage over geological timescales requires assessment of both its geomechanical and geochemical character and how this is affected by the presence of pressurised, CO_2-rich fluid.

Due to the great degree of anisotropy within the Sola and Rodby Shale, caused by the pervasive laminations throughout the shale units, the geomechanical properties of the shales vary substantially as a function of orientation. As shown in the Section 4.2.1, the tensile strength of the shales is far greater when the principal stress acts perpendicular to the shale laminations and is far weaker when the principal stress acts parallel to the laminations.

Once CO_2 injection operations are underway and the CO_2 has entered the sandstone reservoir, it will behave buoyantly, owing to its lower density compared to the formation waters. This will result in the creation of a plume of pressurised supercritical CO_2 / water mix that will eventually accumulate at the reservoir-caprock interface. If this CO_2 plume exerts enough buoyancy pressure upon the reservoir-caprock interface then the capillary entry pressure, or tensile strength, of the caprock may be overcome, resulting in leakage (Busch et al., 2016; Busch and Amann-Hildenbrand, 2013). However, dissipation of this plume, as it travels upwards and outwards from the injection site into the reservoir, as well as interactions with lithological baffles within the Captain Sandstone, i.e. the Sola Shale and calcite-cemented doggers, the pressure of the CO_2 will likely be well below hydrostatic or even pre-hydrocarbon production levels once it has reached the reservoir-caprock interface.

From a geochemical perspective the Sola and Rodby Shales, being dominantly composed of smectite, kaolinite and chlorite, may be susceptible to CO_2 interactions, particularly adsorption causing swelling, or dewatering causing contraction of the caprock. CO_2 adsorption experiments performed by Busch et al. (2008) on a variety of clay minerals at 20 MPa and 50 °C, found that in calcium-exchanged smectite, followed by sodium-exchanged smectite, illite, kaolinite and chlorite, CO_2 was adsorbed in considerable quantities, up to 1 mmol/g. Further experimental work by de Jong et al. (2014) showed that CO_2 penetration of a smectitic caprock would result in adsorption and volume increase by a few percent, 2.46 ± 0.45 % at a CO_2 pressure of 15 MPa and 45 °C, thus closing small fractures and reducing bulk permeability in the effected zone. This swelling depends heavily on the initial hydration state of the smectite, with fully-dehydrated smectite showing little swelling behaviour on exposure to CO_2 due to a smaller spacing between the smectite sheet-like molecular structures not allowing CO_2 to adsorb.

Experiments on caprock corrosion by Armitage et al. (2013) on siltstone from the Krechba gas field, part of the Algerian In Salah CO_2 Storage Project, proposed that the passage of CO_2 through the caprock resulted in dissolution of siderite ($FeCO_3$) and chlorite (Fe-Mg-Al clay) from pore spaces and pore throats, resulting in an increase of

permeability by an order of magnitude. The Rodby Shale contains calcite (0 to 24 %), another carbonate mineral, and chlorite (0 to 3 %), both of which may undergo dissolution in contact with CO_2 in the subsurface. However, the interplay between the dissolution (e.g. carbonate minerals and chlorite) or swelling (e.g. smectite, illite kaolinite, etc.) of minerals in the Acorn CO_2 Storage Site caprock will likely favour swelling processes, due to the high content of swelling clays (26 to 45 %), closing pore volume opened during dissolution and mitigating any permeability increase. Also, of note is that within the Rodby Shale calcite occurs as isolated bioclasts within the clay mineral matrix. In this case dissolution would likely be limited as permeable pathways / pore space does not exist between respective bioclasts meaning flow through of CO_2 is unlikely. A geochemical study on the rate of dissolution of throughgoing, calcite-filled fractures and faults through a caprock were performed by Shell (2015b) for the Peterhead CCS Project. It was found that, under worse case scenarios, it would take 200,000 years for the caprock to be breached via calcite dissolution below the gas-water contact, and then only brine leakage would occur. Above the gas-water contact, if calcite dissolution were to occur then there would be no effective transport mechanisms to move the dissolved calcite away from the caprock.

Another aspect to consider is the in situ dehydration of smectite, if a dry, or near-dry CO_2 plume reached the reservoir-caprock interface. This dewatering of the smectite-bearing shale may occur via pore/interlayer water dissolution in the CO_2 and could result in the production of dehydration cracks. The propagation and frequency of these cracks within the caprock are dependent on diffusion coefficients, plume saturation and the caprock porosity (Busch et al., 2016). If the injected CO_2 in the Acorn CO_2 Storage Site is adequately intermixed with the in situ formation waters prior to reaching the reservoir-caprock interface clay mineral dehydration should not be an issue.

The potential of a localised, pressurised CO_2 plume at the reservoir-caprock contact coupled with the adsorption and swelling of the clay minerals within the caprock may be sufficient to generate differential stresses around the affected area. This could result in shear failure along pre-existing, favourably oriented faults, if present, or along weak lithological planes, such as shale laminations. The chance of leakage during such an occurrence depends on a variety of factors including: the extent of the faulted surface, its mineralogy, the sustained over-pressurisation and the effective normal stress. However, even if shear failure were to occur along a plane of weakness in the caprock a number of mechanical processes would likely take place that would reduce permeability and porosity and mitigate any leakage. Experiments involving triaxial shearing of quartz-kaolinite mixtures of varying proportions performed by Crawford et al. (2008), showed that in clay-rich specimens, after initial hydrostatic loading up to 50 MPa, a ten-fold drop in permeability occurred after shearing to a shear strain of 5. Tembe et al. (2010) also performed triaxial shearing experiments on quartz-clay mixtures and found that during shear of clay-rich specimens the clay minerals became oriented parallel to the direction of shear forming a pervasive foliation, which would likely serve to reduce permeability along the shearing surface. A combination of these processes likely takes place during clay smear along fault planes, a phenomena which has been long understood to reduce permeability and thus fluid flow along fault planes that cut across or are within clay-rich, shale lithologies (Egholm et al., 2008).

6. Summary and conclusions

A novel experimental geomechanical and petrographic investigation was performed on the lithologies of the Acorn CO_2 Storage Site; the Captain Sandstone reservoir, the Rodby Shale caprock and the mid-reservoir Sola Shale. This involved the experimental measurement of tensile strength and yield behaviour at different fluid pressures and specimen porosity, in combination with a variety of analytical techniques to characterise the petrographic character of the lithologies. The analyses presented indicate the suitability of the Acorn CO_2 Storage Site for the proposed CO_2 storage project. The integrated methodologies presented within this study have the potential to be employed at other CO_2 storage sites to provide assurance and reduce risk.

1 The Captain Sandstone is composed predominantly of sub-angular to sub-rounded quartz (81.3 %), plagioclase (5.8 %) and feldspar (6.4 %) grains, with minor carbonate (1.3 %) and clay minerals (2.9 %). The sandstone is moderately to poorly sorted, grain sizes of 50 to 500 μm diameter, with a homogenous structure and high porosity (average 27.5 %). Within both the gas and water-legs, the Captain Sandstone has a low tensile strength, with an average of 0.16 ± 0.013 MPa. These tensile strengths correlate well with the core analysis porosity of the sandstone; high porosity and thus a low degree of cementation, result in low tensile strengths. Stronger horizons exist throughout the sandstone, including calcite-cemented doggers, < 3 m thick with porosities of ~ 5.9 %, and oil-saturated sandstones. They do not compose a substantial portion of the rock and represent a net to gross consideration rather than a reservoir quality issue.
2 Yield curve tests on the Captain Sandstone have shown that permanent, inelastic hydrostatic compaction is achieved at effective pressures of 78 to 110 MPa. The geomechanical behaviour of the sandstone, once hydrostatic compactive yield is achieved, is variable; some specimens show an immediate strengthening with overconsolidation/porosity reduction while other specimens undergo an initial post-compaction weakening and then strengthening once hydrostatically overconsolidated by an additional ~ 20 MPa.
3 The Rodby Shale Caprock is predominately composed of very fine-grained clay minerals, smectite (35.6 %), kaolinite (4.8 %), and chlorite (1.7 %) with some fine-grained quartz (22.1 %), plagioclase (8.6 %) and K-feldspar (5.0 %) grains and calcite occurring as bioclasts (0 to 24.0 %). The mid-reservoir Sola Shale is also predominately composed of very fine-grained clay minerals, smectite (26.3 %), kaolinite (10.3 %), and chlorite (3.3 %) with some fine-grained quartz (32.0 %), plagioclase (11.0 %) and K-feldspar (6.7 %) grains. These shales are finely laminated, with beds that have a thickness of 500 to 1000 μm with fine-grained horizons interbedded within the Captain Sandstone exhibiting intensive bioturbation. Tensile strengths of the Sola/Rodby Shale are typical for shales and vary according to the orientation of the test specimen, with average tensile strengths of 2.4 MPa at horizontal; 0.23 MPa at vertical and 1.22 MPa at parallel orientations. These shales have an average porosity of 13.8 %, an average permeability of 2.2×10^{-19} m^2 (225 nD) and an average tortuosity of 3320.6.
4 The Acorn CO_2 Storage Site lithologies are appropriate for the injection and storage of CO_2. The Captain Sandstone is highly porous and transmissible and its bulk mineralogy is stable under CO_2-rich conditions making it ideal for receiving and containing the proposed quantities of CO_2, 152 MT (up to 5 MT/yr injection rate) for storage for a minimum of 1000 years after cessation of injection, as part of the ACT Acorn Development Plan. The proposed injection pressures, of 4.5 to 16 MPa, will be accommodated by the lithologies without rock failure and disaggregation. The shale caprock similarly has a suitable mineralogy and geomechanical character for long-term CO_2 storage.
5 However, due to the high porosity and low cementation the Captain Sandstone, it is vulnerable to disaggregation and porosity-reduction if stress/pressure conditions in the near wellbore exceed its yield strength. Mitigation measures, if failure were to occur, may be required, such as the use of gravel packers and sand screens in the wellbore infrastructure. The Rodby Shale caprock, due to its high swelling clay content, may be vulnerable to either CO_2 adsorption and swelling or dewatering, the former increasing caprock integrity via closure of leakage pathways while the former may facilitate CO_2 penetration into the caprock as progressive dewatering of the

swelling clay takes place.

6 Deformation analysis in reservoir space (DARS) analyses indicate that during the initial injection of CO_2 the stress/pressure conditions within the near wellbore will move towards, but not exceed, the tensile failure yield surface and the overburden stress. This leads us to conclude that the rock in the near wellbore environment should remain intact and pressures will rapidly reduce as the CO_2 dissipates into the highly permeable and porous reservoir.

CRediT authorship contribution statement

Michael J. Allen: Conceptualization, Methodology, Validation, Formal analysis, Investigation, Resources, Data curation, Writing - original draft, Visualization, Supervision, Project administration. **Daniel R. Faulkner:** Conceptualization, Methodology, Validation, Resources, Writing - review & editing, Supervision, Project administration, Funding acquisition. **Richard H. Worden:** Conceptualization, Methodology, Validation, Resources, Writing - review & editing, Supervision, Project administration, Funding acquisition. **Elliot Rice-Birchall:** Investigation. **Nikolaos Katirtsidis:** Investigation. **James E.P. Utley:** Investigation, Validation.

Declaration of Competing Interest

There are no conflicts of interest associated with this article.

Acknowledgements

This investigation was instigated by ACT Acorn project (project 271500), funded by the Department for Business, Energy and Industrial Strategy, United Kingdom; the Research Council of Norway; Netherlands Enterprise Agency; and ERA-NET under the Horizon 2020 programme.

We would like to thank all those involved in the ACT-ACORN CCS Project, including Alan James, Hazel Robertson, Steve Murphy and Tim Dumenil of Pale Blue Dot Energy; Juan Alcalde and Claire Bond of the University of Aberdeen; Niklas Heinemann of the University of Edinburgh; Saeed Ghanbari and Eric Mackay of Herriot-Watt University; Gary Coughlan for technical assistance during laboratory analyses; CNOOC-Nexen Petroleum UK Ltd for allowing sampling of wells 14/26-1, 14/26a-6, 14/26a-7A and 14/26a-8; and Repsol Sinopec Resources UK Ltd for allowing sampling of well 13/30-3.

Appendix A

Table A1
Locations and basic information of the wells sampled in this study.

Well	13 / 30-3
Location	58°03'51.60"N ; 01°04'37.96"W
Total Measured Depth - MD (m)	3602.74
Core 1 (m - MD)	2004.67–2016.8
Core 2 (m - MD)	6617.1–2043.02
Core 3 (m - MD)	3503.1–3515.62
Gas - Oil Contact (m - MD)	2000.40
Oil - Water Contact (m - MD)	2002.84
Well	**14 / 26-1**
Location	58°01'54.187"N ; 00°54'39.171"W
Total Measured Depth - MD (m)	2641.09
Core 1 (m - MD)	1990.34–1996.14
Core 2 (m - MD)	1996.14–2005.58
Core 3 (m - MD)	2005.58–2013.51
Core 4 (m - MD)	2027.53–2044.9
Gas - Water Contact (m - MD)	1989.12
Well	**14 / 26a-6**
Location	58°01'12.28'N ; 00°54'39.85"W
Total Measured Depth - MD (m)	2147.93
Core 1 (m - MD)	1971.14–1978.76
Core 2 (m - MD)	1978.76–1994.61
Gas - Water Contact (m - MD)	1992.45
Well	**14 / 26a-7A**
Location	58°02'15.02'N ; 00°53'22.17"W
Total Measured Depth - MD (m)	2177.96
Core 1 (m - MD)	1976.93–2005.28
Gas - Oil contact (m - MD)	1994.31
Oil - Water contact (m - MD)	1996.44
Well	**14 / 26a-8**
Location	58°00'24.977'N ; 00°52'26.581"W
Total Measured Depth - MD (m)	2278.08
Core 1 (m - MD)	1947.67–1974.49
Core 2 (m - MD)	1975.10–2002.54
Core 3 (m - MD)	2002.84–2030.27
Gas - Oil Contact (m - MD)	1997.05
Oil - Water Contact (m - MD)	1999.49

Appendix B. Supplementary data

Supplementary data associated with this article can be found, in the online version, at https://doi.org/10.1016/j.ijggc.2019.102923.

References

Ahmadi, Z., Sawyers, M., Kenyon-Roberts, S., Stanworth, B., Kugler, K., Kristensen, J., Fugelli, E., 2003. Paleocene. In: Evans, D., Graham, C., Armour, A., Bathurst, P. (Eds.), The Millenium Atlas. Petroleum Geology of the Central and Northern North Sea pp. 14-1-14–49.

Alcade, J., Heinemann, N., Mabon, L., Worden, R.H., de Coninck, H., Robertson, H., Maver, M., Ghanbari, S., Swennenhuis, F., Mann, I., Walker, T., Gomersal, S., Bond, C.E., Allen, M.J., Haszeldine, R.S., James, A., Mackay, E.J., Brownsort, P.A., Faulkner, D.R., Murphy, S., 2019. Acorn: developing full-chain industrial carbon capture and storage in a resource- and infrastructure-rich hydrocarbon province. J. Clean. Prod xx, xx.

Antonellini, M.A., Aydin, A., Pollard, D.D., 1994. Microstructure of deformation bands in porous sandstones at Arches National Park. Utah. J. Struct. Geol. 16, 941–959. https://doi.org/10.1016/0191-8141(94)90077-9.

Argent, J.D., Stewart, S.A., Green, P.F., Underhill, J.R., 2002. Heterogeneous exhumation in the Inner Moray Firth, UK North Sea: constraints from new AFTA(R) and seismic data. J. Geol. Soc. https://doi.org/10.1144/0016-764901-141.

Armitage, P.J., Faulkner, D.R., Worden, R.H., 2013. Caprock corrosion. Nat. Geosci. 6, 79–80. https://doi.org/10.1038/ngeo1716.

Armitage, P.J., Worden, R.H., Faulkner, D.R., Aplin, A.C., Butcher, A.R., Iliffe, J., 2010. Diagenetic and sedimentary controls on porosity in Lower Carboniferous fine-grained lithologies, Krechba field, Algeria: a petrological study of a caprock to a carbon capture site. Mar. Pet. Geol. 27, 1395–1410. https://doi.org/10.1016/j.marpetgeo.2010.03.018.

ASTM D3967-16, 2016. Standard Test Method for Splitting Tensile Strength of Intact Rock Core Specimens. ASTM International, West Conshohocken, PA. https://doi.org/10.1520/D3967-16.

Aydin, A., Johnson, A.M., 1978. Development of faults as zones of deformation bands and as slip surfaces in sandstone. Pure Appl. Geophys. 116, 931–942. https://doi.org/10.1007/BF00876547.

Ballas, G., Soliva, R., Sizun, J.-P., Fossen, H., Benedicto, A., Skurtveit, E., 2013. Shear-enhanced compaction bands formed at shallow burial conditions; implications for fluid flow (Provence, France). J. Struct. Geol. 47, 3–15. https://doi.org/10.1016/j.jsg.2012.11.008.

Barton, C.A., Zoback, M.D., Burns, K.L., 1988. In-situ stress orientation and magnitude at the Fenton Geothermal Site, New Mexico, determined from wellbore breakouts. Geophys. Res. Lett. 15, 467–470. https://doi.org/10.1029/GL015i005p00467.

Baud, P., Klein, E., Wong, T.F., 2004. Compaction localization in porous sandstones: spatial evolution of damage and acoustic emission activity. J. Struct. Geol. 26, 603–624. https://doi.org/10.1016/j.jsg.2003.09.002.

Baud, P., Schubnel, A., Wong, T., 2000a. Dilatancy,compaction, and failure mode in Solnhofen limestone. J. Geophys. Res. 105, 289–303. https://doi.org/10.1029/2000JB900133.

Baud, P., Vajdova, V., Wong, T., 2006. Shear-enhanced compaction and strain localization: inelastic deformation and constitutive modeling of four porous sandstones. J. Geophys. Res. Solid Earth 111. https://doi.org/10.1029/2005JB004101.

Baud, P., Vinciguerra, S., David, C., Cavallo, A., Walker, E., Reuschlé, T., 2009. Compaction and failure in high porosity carbonates: mechanical data and microstructural observations. Pure Appl. Geophys. 166, 869–898. https://doi.org/10.1007/s00024-009-0493-2.

Baud, P., Zhu, W., Wong, T., 2000b. Failure mode and weakening effect of water on sandstone. J. Geophys. Res. Solid Earth 105, 16371–16389. https://doi.org/10.1029/2000JB900087.

Bedford, J.D., Faulkner, D.R., Leclère, H., Wheeler, J., 2018. High-resolution mapping of yield curve shape and evolution for porous rock: the effect of inelastic compaction on porous bassanite. J. Geophys. Res. Solid Earth 123, 1217–1234. https://doi.org/10.1002/2017JB015250.

Bedford, J.D., Faulkner, D.R., Wheeler, J., Leclère, H., 2019. High-resolution mapping of yield curve shape and evolution for high porosity sandstone. J. Geophys. Res. Solid Earth 124, xx.

Bratton, T., Bricout, V., Lam, R., Plona, T., Sinha, B., Tagbor, K., Venkitaraman, A., Borbas, T., 2004. Rock strength parameters from annular pressure while drilling and dipole sonic dispersion analysis. SPWLA 45th Annu. Logging Symp.

Busch, A., Alles, S., Gensterblum, Y., Prinz, D., Dewhurst, D.N., Raven, M.D., Stanjek, H., Krooss, B.M., 2008. Carbon dioxide storage potential of shales. Int. J. Greenh. Gas Control 2, 297–308. https://doi.org/10.1016/j.ijggc.2008.03.003.

Busch, A., Amann-Hildenbrand, A., 2013. Predicting capillarity of mudrocks. Mar. Pet. Geol. 45, 208–223. https://doi.org/10.1016/j.marpetgeo.2013.05.005.

Busch, A., Bertier, P., Gensterblum, Y., Rother, G., Spiers, C.J., Zhang, M., Wentinck, H.M., 2016. On sorption and swelling of CO2 in clays. Geomech. Geophys. Geo-Energy Geo-Resources 2, 111–130. https://doi.org/10.1007/s40948-016-0024-4.

Byerlee, J.D.D., 1978. Friction of rocks. Pure and Applied Geophysics PAGEOPH. https://doi.org/10.1007/BF00876528.

Chan, A.W., Zoback, M.D., 2002. Deformation analysis in reservoir space (DARS): a simple formalism for prediction of reservoir deformation with depletion. SPE/ISRM Rock Mech. Conf. https://doi.org/10.2118/78174-MS.

Cilona, A., Faulkner, D.R., Tondi, E., Agosta, F., Mancini, L., Rustichelli, A., Baud, P., Vinciguerra, S., 2014. The effects of rock heterogeneity on compaction localization in porous carbonates. J. Struct. Geol. 67, 75–93. https://doi.org/10.1016/j.jsg.2014.07.008.

Copestake, P., Sms, A.P., Crittenden, S., Hamar, G.P., Ineson, J.R., Rose, P.T., Tringham, M.E., 2003. Lower cretaceous. In: Evans, D., Graham, C., Armour, A., Bathurst, P. (Eds.), The Millenium Atlas. Petroleum Geology of the Central and Northern North Sea pp. 12-1-12–48.

Crawford, B.R., Faulkner, D.R., Rutter, E.H., 2008. Strength, porosity, and permeability development during hydrostatic and shear loading of synthetic quartz-clay fault gouge. J. Geophys. Res. Solid Earth 113. https://doi.org/10.1029/2006JB004634.

Curran, J., Carroll, M., 2018. Shear stress enhancement of void compaction. J. Geophys. Res. Solid Earth 84, 1105–1112. https://doi.org/10.1029/JB084iB03p01105.

Cuss, R.J., Rutter, E.H., Holloway, R.F., 2003a. Experimental observations of the mechanics of borehole failure in porous sandstone. Int. J. Rock Mech. Min. Sci. 40, 747–761. https://doi.org/10.1016/S1365-1609(03)00068-6.

Cuss, R.J., Rutter, E.H., Holloway, R.F., 2003b. The application of critical state soil mechanics to the mechanical behaviour of porous sandstones. Int. J. Rock Mech. Min. Sci. 40, 847–862. https://doi.org/10.1016/S1365-1609(03)00053-4.

de Jong, S.M., Spiers, C.J., Busch, A., 2014. Development of swelling strain in smectite clays through exposure to carbon dioxide. Int. J. Greenh. Gas Control 24, 149–161. https://doi.org/10.1016/j.ijggc.2014.03.010.

Dresen, G., Stanchits, S., Rybacki, E., 2010. Borehole breakout evolution through acoustic emission location analysis. Int. J. Rock Mech. Min. Sci. 47, 426–435. https://doi.org/10.1016/j.ijrmms.2009.12.010.

Egholm, D.L., Clausen, O.R., Sandiford, M., Kristensen, M.B., Korstgård, J.A., 2008. The mechanics of clay smearing along faults. Geology 36, 787–790. https://doi.org/10.1130/G24975A.1.

Faulkner, D.R., Armitage, P.J., 2013. The effect of tectonic environment on permeability development around faults and in the brittle crust. Earth Planet. Sci. Lett. https://doi.org/10.1016/j.epsl.2013.05.006.

Fisher, Q.J., Casey, M., Clennell, M.B., Knipe, R.J., 1999. Mechanical compaction of deeply buried sandstones of the North Sea. Mar. Pet. Geol. 16, 605–618. https://doi.org/10.1016/S0264-8172(99)00044-6.

Fraser, S.I., Robinson, A.M., Johnson, H.D., Underhill, J.R., Kadolsky, D.G.A., Connell, R., Johannesen, P., Ravnås, R., 2003. Upper jurassic. In: Evans, D., Graham, C., Armour, A., Bathurst, P. (Eds.), The Millennium Atlas: Petroleum Geology of the Central and Northern North Sea, pp. 157–189.

Fyfe, A., Gregersen, U., Jordt, H., Rundberg, Y., Eidvin, T., Evans, D., Stewart, D., Hovland, M., Andresen, P., 2003. Oligocene to holocene. In: Evans, D., Graham, C., Armour, A., Bathurst, P. (Eds.), The Millenium Atlas. Petroleum Geology of the Central and Northern North Sea pp. 16-1-16–32.

Gallois, R.W., 2004. The Kimmeridge Clay: the most intensively studied formation in Britain. Open Univ. Geol. J.

Garrett, S.W., Atherton, T., Hurst, A., 2000. Lower cretaceous deep-water sandstone reservoirs of the UK Central North Sea. Pet. Geosci. 6, 231–240.

Griffiths, J., Faulkner, D.R., Edwards, A.P., Worden, R.H., 2018. Deformation band development as a function of intrinsic host-rock properties in Triassic Sherwood Sandstone. Geol. Soc. London, Spec. Publ. 435 161 LP – 176.

Guariguata-Rojas, G.J., Underhill, J.R., 2017. Implications of Early Cenozoic uplift and fault reactivation for carbon storage in the Moray Firth Basin. Interpretation 5, SS1–SS21. https://doi.org/10.1190/INT-2017-0009.1.

Guéguen, Y., Palciauskas, V., 1994. Mechanical Behavior of Fluid-Saturated Rocks, in: Introduction to the Physics of Rocks. Princeton University Press, Princeton, New Jersey.

Haimson, H.C., Herrick, C.G., 1986. Borehole breakouts - a new tool for estimating in situ stress? ISRM Int. Symp.

Hangx, S.J.T., Spiers, C.J., Peach, C.J., 2010. Creep of simulated reservoir sands and coupled chemical-mechanical effects of CO2injection. J. Geophys. Res. Solid Earth 115. https://doi.org/10.1029/2009JB006939.

Hannis, S., Bricker, S., Goater, A., Holloway, S., Rushton, J., Williams, G., Williams, J., 2013. Cross-international boundary effects of CO2 injection. Energy Procedia 37, 4927–4936. https://doi.org/10.1016/j.egypro.2013.06.404.

Heling, D., 1970. MICRO-FABRICS of Shales and their rearrangement by COMPACTION. Sedimentology 15, 247–260. https://doi.org/10.1111/j.1365-3091.1970.tb02188.x.

Hillier, S., 2009. Quantitative analysis of clay and other minerals in sandstones by X-Ray powder diffraction (XRPD). Clay Miner. Cem. Sandstones. https://doi.org/10.1002/9781444304336.ch11. Wiley Online Books.

Hillier, S., 2000. Accurate quantitative analysis of clay and other minerals in sandstones by XRD: comparison of a Rietveld and a reference intensity ratio (RIR) method and the importance of sample preparation. Clay Miner. 35, 291–302.

Hillis, R.R., Nelson, E.J., 2005. In situ stresses in the North Sea and their applications: petroleum geomechanics from exploration to development. Geol. Soc. London, Pet. Geol. Conf. Ser. 6, 551–564. https://doi.org/10.1144/0060551.

Hillis, R.R., Thomson, K., Underhill, J.R., 1994. Quantification of Tertiary erosion in the Inner Moray Firth using sonic velocity data from the Chalk and the Kimmeridge Clay. Mar. Pet. Geol. https://doi.org/10.1016/0264-8172(94)90050-7.

Hoffman, N., Collins, G., Castillo, D., 2017. Principles for Best Practice Geomechanics for CCS Injection Operations and Its Application to the CarbonNet Project.

Huang, Y.-H., Yang, S.-Q., Hall, M., Zhang, Y.-C., 2018. The effects of NaCl concentration and confining pressure on mechanical and acoustic behaviors of brine-saturated sandstone. Energies 11, 385. https://doi.org/10.3390/en11020385.

Jaeger, J.C., Cook, N.G.W., Zimmerman, R., 2007. Fundamentals of Rock Mechanics, fourth edi. Wiley-Blackwell, London.

Jin, M., Mackay, E., Quinn, M., 2012. Evaluation of the CO_2 storage capacity of the captain sandstone formation. SPE Eur. Annu. Conf. Exhib. SPE. https://doi.org/10.2118/154539-MS. 154539.

Jones, E., Jones, B., Ebdon, C., Ewen, D., Milner, P., Plunkett, J., Hudson, G., Slater, P.,

2003. Eocene. In: Evans, D., Graham, C., Armour, A., Bathurst, P. (Eds.), The Millenium Atlas. Petroleum Geology of the Central and Northern North Sea pp. 15-1-15–31.
Kirsch, E.G., 1898. Die theorie der elastizität und die Bedürfnisse Der Festigkeitslehre. Zeitschrift des Vereines Dtsch. Ingenieure 42, 797–807.
Kubala, M., Bastow, M., Thompson, S., Scotchman, I., Øygard, K., 2003. Geothermal regime, petroleum generation and migration. The Geological Society of London.
Louis, L., Baud, P., Wong, T., 2009. Microstructural inhomogeneity and mechanical anisotropy associated with bedding in Rothbach Sandstone. Pure Appl. Geophys. 166, 1063–1087. https://doi.org/10.1007/s00024-009-0486-1.
Makowitz, A., Milliken, K.L., 2003. Quantification of brittle deformation in burial compaction, Frio and mount simon formation sandstones. J. Sediment. Res. A Sediment. Petrol. Process. 73, 1007–1021.
Mathisen, A.M., Aastveit, G.L., Alteraas, E., 2007. Successful Installation of Stand Alone Sand Screen in more than 200 Wells - the Importance of Screen Selection Process and Fluid Qualification. Eur. Form. Damage Conf. https://doi.org/10.2118/107539-MS.
McDermott, C., Williams, J., Tucker, O., Jin, M., Mackay, E., Edlmann, K., Haszeldine, R.S., Wang, W., Kolditz, O., Akhurst, M., 2016. Screening the geomechanical stability (thermal and mechanical) of shared multi-user CO2storage assets: a simple effective tool applied to the Captain Sandstone Aquifer. Int. J. Greenh. Gas Control 45, 43–61. https://doi.org/10.1016/j.ijggc.2015.11.025.
Menéndez, B., Zhu, W., Wong, T.-F., 1996. Micromechanics of brittle faulting and cataclastic flow in Berea sandstone. J. Struct. Geol. 18, 1–16. https://doi.org/10.1016/0191-8141(95)00076-P.
Nagel, N.B., 2001. Compaction and subsidence issues within the petroleum industry: from wilmington to ekofisk and beyond. Phys. Chem. Earth, Part A Solid Earth Geod. 26, 3–14. https://doi.org/10.1016/S1464-1895(01)00015-1.
Oakman, C., 2005. The Lower Cretaceous plays of the Central and Northern North Sea: Atlantean drainage models and enhanced hydrocarbon potential. Geol. Soc. London, Pet. Geol. Conf. Ser. 6https://doi.org/10.1144/0060187. 187 LP – 198.
Pale Blue Dot Energy, 2018a. ACT Acorn D07 Acorn CO2 Storage Site Development Plan. ACT Acorn Consortium.
Pale Blue Dot Energy, 2018b. Full Chain Development Plan and Budget.
Pale Blue Dot Energy and Axis Well Technology, 2016a. Progressing Development of the UK's Strategic Carbon Dioxide Storage Resource: a Summary of Results from the Strategic UK CO2 Storage Appraisal Project.
Pale Blue Dot Energy and Axis Well Technology, 2016b. Energy Technologies Institute Strategic UK CCS Storage Appraisal Project - Captain X site Storage Development Plan.
Pijnenburg, R.P.J., Verberne, B.A., Hangx, S.J.T., Spiers, C.J., 2019. Inelastic deformation of the slochteren sandstone: stress-strain relations and implications for induced seismicity in the Groningen Gas Field. J. Geophys. Res. Solid Earth 124, 5254–5282. https://doi.org/10.1029/2019JB017366.
Pinnock, S., Clitheroe, A., Rose, P., 2003. The Captain Field, Block 13/22a, UK North Sea. Geol. Soc. London, Mem. 20, 431–441.
Pirrie, D., Butcher, A.R., Power, M.R., Gottlieb, P., Miller, G.L., 2004. Rapid quantitative mineral and phase analysis using automated scanning electron microscopy (QemSCAN); potential applications in forensic geoscience. Geol. Soc. London, Spec. Publ. 232https://doi.org/10.1144/GSL.SP.2004.232.01.12. 123 LP – 136.
Richardson, N.J., Allen, M.R., Underhill, J.R., 2005. Role of Cenozoic fault reactivation in controlling pre-rift plays, and the recognition of Zechstein Group evaporite-carbonate lateral facies transitions in the East Orkney and Dutch Bank basins, East Shetland Platform, UK North Sea. Geol. Soc. London, Pet. Geol. Conf. Ser. 6https://doi.org/10.1144/0060337. 337 LP – 348.
Rider, M., 2002. The Geological Interpretation of Well Logs. Rider-French Consult. Ltdhttps://doi.org/10.1088/0960-1317/18/10/104006.
Ringrose, P.S.S., Mathieson, A.S.S., Wright, I.W.W., Selama, F., Hansen, O., Bissell, R., Saoula, N., Midgley, J., 2013. The In Salah CO_2 Storage Project: Lessons Learned and Knowledge Transfer. Energy Procedia 37, 6226–6236. https://doi.org/10.1016/j.egypro.2013.06.551.
Rutter, E.H., Glover, C.T., 2012. The deformation of porous sandstones; are Byerlee friction and the critical state line equivalent? J. Struct. Geol. https://doi.org/10.1016/j.jsg.2012.08.014.
Rutter, E.H., Llana-Fúnez, S., Brodie, K.H., 2009. Dehydration and deformation of intact cylinders of serpentinite. J. Struct. Geol. 31, 29–43. https://doi.org/10.1016/j.jsg.2008.09.008.
Schlumberger, 2018. Fracture Gradient [WWW Document]. URL. Oilf. Gloss. http://www.glossary.oilfield.slb.com/Terms/f/fracture_gradient.aspx.
Scottish Carbon Capture and Storage, Shell, The Crown Estate, Scottish Government, Scottish Enterprise, Vattenfall, 2015. CO2Multistore: Optimising CO2 Storage in Geological Formations; A Case Study Offshore Scotland.
ScottishPower CCS Consortium, 2010. Longannet FEED work, UK Carbon Capture and Storage Demonstration Competition. FEED Close Out Report.
Segall, P., 1985. Stress and subsidence resulting from subsurface fluid withdrawal in the epicentral region of the 1983 Coalinga Earthquake. J. Geophys. Res. Solid Earth 90, 6801–6816. https://doi.org/10.1029/JB090iB08p06801.
Shell, 2015a. Peterhead CCS Project.
Shell, 2015b. Geochemical Reactivity Report. Peterhead Project UK Carbon Capture and Storage Demonstration Competition Report. PCCS-05-PT-ZR-3323-00001. .
Sulak, A.M., Danielsen, J., 1988. Reservoir Aspects Of Ekofisk Subsidence. Offshore Technol. Conf. https://doi.org/10.4043/5618-MS.
Surlyk, F., Dons, T., Clausen, C.K., Higham, J., 2003. Upper cretaceous. In: Evans, D., Graham, C., Armour, A., Bathurst, P. (Eds.), The Millenium Atlas: Petroleum Geology of the Central and Northern North Sea, pp. 13-1-13–58.
Tembe, S., Baud, P., Wong, T.F., 2008. Stress conditions for the propagation of discrete compaction bands in porous sandstone. J. Geophys. Res. Solid Earth 113. https://doi.org/10.1029/2007JB005439.
Tembe, S., Lockner, D., Wong, T.F., 2010. Effect of clay content and mineralogy on frictional sliding behavior of simulated gouges: binary and ternary mixtures of quartz, illite, and montmorillonite. J. Geophys. Res. https://doi.org/10.1029/2009JB006383.
Thienen-Visser, K.P., Pruiksma, J.N., Breunese, J., 2015. Compaction and subsidence of the Groningen gas field in the Netherlands. Proceedings of the International Association of Hydrological Sciences. https://doi.org/10.5194/piahs-372-367-2015.
Vasco, D.W., Rucci, A., Ferretti, A., Novali, F., Bissell, R.C., Ringrose, P.S., Mathieson, A.S., Wright, I.W., 2010. Satellite-based measurements of surface deformation reveal fluid flow associated with the geological storage of carbon dioxide. Geophys. Res. Lett. 37. https://doi.org/10.1029/2009GL041544.
Veronika, V., Patrick, B., Wong, T.F., 2004. Compaction, dilatancy, and failure in porous carbonate rocks. J. Geophys. Res. Solid Earth 109. https://doi.org/10.1029/2003JB002508.
Wei, Z., Patrick, B., Sergio, V., Teng-fong, W., 2011. Micromechanics of brittle faulting and cataclastic flow in Alban Hills tuff. J. Geophys. Res. Solid Earth 116. https://doi.org/10.1029/2010JB008046.
White, A.J., Traugott, M.O., Swarbrick, R.E., 2002. The use of leak-off tests as means of predicting minimum in-situ stress. Pet. Geosci. 8 189 LP – 193.
Williams, J.D.O., Fellgett, M.W., Kingdon, A., Williamson, J.P., 2015. In-situ stress orientations in the UK Southern North Sea: regional trends, deviations and detachment of the post-Zechstein stress field. Mar. Pet. Geol. 67, 769–784. https://doi.org/10.1016/j.marpetgeo.2015.06.008.
Williams, J.D.O., Fellgett, M.W., Quinn, M.F., 2016. Carbon dioxide storage in the Captain Sandstone aquifer: determination of in situ stresses and fault-stability analysis. Pet. Geosci. 22, 211–222. https://doi.org/10.1144/petgeo2016-036.
Wong, T., Baud, P., 2012. The brittle-ductile transition in porous rock: a review. J. Struct. Geol. 44, 25–53. https://doi.org/10.1016/j.jsg.2012.07.010.
Wong, T., Christian, D., Wenlu, Z., 1997. The transition from brittle faulting to cataclastic flow in porous sandstones: mechanical deformation. J. Geophys. Res. Solid Earth 102, 3009–3025. https://doi.org/10.1029/96JB03281.
Wooldridge, L.J., Worden, R.H., Griffiths, J., Utley, J.E.P., Thompson, A., 2018. The origin of clay-coated sand grains and sediment heterogeneity in tidal flats. Sediment. Geol. 373, 191–209. https://doi.org/10.1016/j.sedgeo.2018.06.004.
Worden, R.H., Burley, S.D., 2003. Sandstone Diagenesis: The Evolution of Sand to Stone, Sandstone Diagenesis: Recent and Ancient. Wiley Online Bookshttps://doi.org/10.1002/9781444304459.ch.
Zanella, E., Coward, M.P., 2003. Structural framework. In: Evans, D., Graham, C., Armour, A., Bathhusrt, P. (Eds.), The Millennium Atlas: Petroleum Geology of the Central and Northern North Sea. Geological Society, London, London, pp. 45–59.
Zhang, J., Yin, S.-X., 2017. Fracture gradient prediction: an overview and an improved method. Pet. Sci. 14, 720–730. https://doi.org/10.1007/s12182-017-0182-1.
Zhang, Wong, T.-F., Davis, D.M., 1990. Micromechanics of pressure-induced grain crushing in porous rocks. J. Geophys. Res. 95, 341. https://doi.org/10.1029/JB095iB01p00341.
Zoback, M.D., 2007. Reservoir Geomechanics. Reservoir Geomechanics. https://doi.org/10.1017/CBO9780511586477.
Zoback, M.D., Barton, C.A., Brudy, M., Castillo, D.A., Finkbeiner, T., Grollimund, B.R., Moos, D.B., Peska, P., Ward, C.D., Wiprut, D.J., 2003. Determination of stress orientation and magnitude in deep wells. Int. J. Rock Mech. Min. Sci. 40, 1049–1076. https://doi.org/10.1016/j.ijrmms.2003.07.001.
Zoback, M.D., Daniel, M., Larry, M.N.A.R., 1985. Well bore breakouts and in situ stress. J. Geophys. Res. Solid Earth 10, 5523–5530. https://doi.org/10.1029/JB090iB07p05523.